

Euler's Elastica-Based Cartoon-Smooth-Texture Image Decomposition*

Roy Y. He[†] and Hao Liu[‡]

Abstract. We propose a novel model for decomposing grayscale images into three distinct components: the structural part, representing sharp boundaries and regions with strong light-to-dark transitions; the smooth part, capturing soft shadows and shades; and the oscillatory part, characterizing textures and noise. To capture the homogeneous structures, we introduce a combination of L^0 -gradient and curvature regularization on level lines. This new regularization term enforces strong sparsity on the image gradient while reducing the undesirable staircase effects as well as preserving the geometry of contours. For the smoothly varying component, we utilize the L^2 -norm of the Laplacian that favors isotropic smoothness. To capture the oscillation, we use the inverse Sobolev seminorm. To solve the associated minimization problem, we design an efficient operator-splitting algorithm. Our algorithm effectively addresses the challenging nonconvex nonsmooth problem by separating it into subproblems. Each subproblem can be solved either directly using closed-form solutions or efficiently using the fast Fourier transform. We provide systematic experiments, including ablation and comparison studies, to analyze our model's behaviors and demonstrate its effectiveness as well as efficiency.

Key words. image decomposition, oscillatory-structure cartoon, Euler's elastica energy, operator splitting

MSC codes. 68U10, 94A08, 65D18

DOI. 10.1137/24M167411X

1. Introduction. In many tasks of image processing, such as denoising, segmentation, compression, and pattern analysis, a given image $f : \Omega \rightarrow \mathbb{R}$ defined on a compact domain $\Omega \subset \mathbb{R}^2$ can be written as a sum of several components, each of which represents a distinctive feature of f . For example, the well-known Rudin–Osher–Fatemi (ROF) model [52] separates a noisy image $f = u + n$ into its noise-free part u and the noisy remainder n by considering

$$(1.1) \quad \min_{(u,v) \in \text{BV}(\Omega) \times L^2(\Omega)/f=u+n} \left[\frac{1}{2\lambda} \|n\|_{L^2(\Omega)}^2 + \int_{\Omega} |\nabla u| \right].$$

Here, $\int_{\Omega} |\nabla u|$ is the total variation (TV)-norm of a bounded variation function $u \in \text{BV}(\Omega) = \{u \in L^1(\Omega) : \int_{\Omega} |\nabla u| < +\infty\}$, and $\lambda > 0$ is a weight parameter. Various extensions of the ROF model are proposed in the literature, mainly from two perspectives. The first branch of works is motivated by the fact that the L^2 -norm in (1.1) can fail to capture noise [46, 4], thus leaving visible oscillations in u . Another class of works is based on the observation that the

*Received by the editors July 3, 2024; accepted for publication (in revised form) December 4, 2024; published electronically February 19, 2025.

<https://doi.org/10.1137/24M167411X>

Funding: The work of the first author was partially supported by CityU grant 7200779. The work of the second author was partially supported by National Natural Science Foundation of China grant 12201530 and HKRGC ECS grant 22302123.

[†]Department of Mathematics, City University of Hong Kong, Kowloon Tong, Hong Kong (royhe2@cityu.edu.hk).

[‡]Department of Mathematics, Hong Kong Baptist University, Kowloon Tong, Hong Kong (haoliu@hkbu.edu.hk).

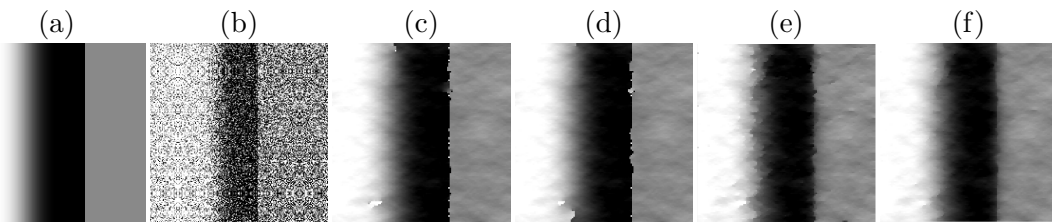


Figure 1. Motivation for curvature regularization on level lines. (a) Clean image. (b) Noisy image ($\sigma = 120/255$). (c) Denoised image by L^0 -gradient. (d) Denoised image by the minimax concave (MC) penalty function [64]. (e) Denoised image by TV. (f) Denoised image by Euler's elastica [47]. The noise is captured by H^{-1} -norm approximating Meyer's G -norm. Observe that the L^0 -gradient and minimax concave (MC) penalty function produce irregular boundaries and the TV-norm creates staircase effects. These artifacts are reduced in (f) when incorporating the curvature regularization on the level lines.

TV-norm leads to various artifacts including staircase effects and loss of geometry as well as contrast [13, 1, 43, 67]. See Figure 1(e) for an illustration.

In his seminal work [46], Meyer suggested characterizing the oscillating patterns of an image including textures and noise by the dual space of the closure of the Schwartz class in $BV(\mathbb{R}^2)$. Later, Aubert and Aujol [4] refined the construction by restricting themselves to the case of an open and bounded domain Ω . They proposed the $G(\Omega)$ -space as a subspace of the dual of the Sobolev space $W_0^{1,1}(\Omega)$ and formulated Meyer's model as

$$(1.2) \quad \min_{(u,v) \in BV(\Omega) \times G(\Omega)/f=u+n} \left[\frac{1}{\lambda} \|v\|_{G(\Omega)} + \int_{\Omega} |\nabla u| \right],$$

where $\|\cdot\|_{G(\Omega)}$ stands for the G -norm. A key property of the G -norm is that oscillating functions converging to 0 in $G(\Omega)$ do not have to converge strongly in $L^2(\Omega)$ [4], which justifies the benefit of using the G -norm in place of the L^2 -norm in the ROF model for noise. Because the G -norm is related to the L^∞ -norm, it is computationally challenging to solve (1.2). Vese and Osher [57] proposed the first practical solution by considering

$$(1.3) \quad \min_{(u,g) \in BV(\Omega) \times (L^p(\Omega))^2} \left[\int_{\Omega} |\nabla u| + \frac{1}{2\lambda} \int_{\Omega} |f - u - \partial_x g_1 - \partial_y g_2|^2 dx + \mu \|g\|_{L^p(\Omega)} \right],$$

where dx stands for the Lebesgue measure in \mathbb{R}^2 , $\lambda > 0$ and $\mu > 0$ are weight parameters, $p \geq 1$ is an integer index, and $\|g\|_{L^p(\Omega)} = \|\sqrt{g_1^2 + g_2^2}\|_{L^p(\Omega)}$ for $g = (g_1, g_2)$. They showed that, as $\lambda \rightarrow 0$ and $p \rightarrow \infty$, $\partial_x g_1 + \partial_y g_2$ belongs to $G(\Omega)$. They derived the Euler–Lagrange equation related to (1.3) and solved the problem after discretization in the case of $p = 1$. In [50], a simplified version of (1.3) when $p = 2$ was studied, which leads to using the $H^{-1}(\Omega)$ -seminorm in place of Meyer's G -norm, where $H^{-1}(\Omega)$ is the dual of $H_0^1(\Omega)$. Approaching from a different perspective, Aujol et al. [5] proposed tackling Meyer's problem by restricting the function space $G(\Omega)$ to a convex subset $G_\mu(\Omega) = \{v \in G(\Omega) \mid \|v\|_{G(\Omega)} \leq \mu\}$ for some $\mu > 0$. Analogous to Chambolle's method [12] for (1.1), a projection algorithm was proposed in [5] to solve their model. In [58], Wen et al. considered the Legendre–Fenchel duality of Meyer's G -norm and proposed a primal-dual algorithm for the cartoon-texture decomposition. In the literature, there are many other types of regularizations for capturing texture and noise. For

instance, the bounded mean oscillation space was considered in [36, 26], the negative Hilbert–Sobolev space H^{-s} was applied in [38], and a general family of Hilbert spaces were studied in [7]. With a more refined decomposition, Aujol and Chambolle [6] suggested separating a digital image f as a sum of three components: the geometric part $u \in \text{BV}(\Omega)$, the texture part $v \in G_\mu(\Omega)$, and the noise component w in the Besov space [46] consisting of functions whose wavelet coefficients are in ℓ^∞ . A fast filter method as well as a nice summary of variational models for cartoon + texture decomposition is available in [11]. These variational decomposition frameworks have also been extended and applied to color images [8, 37, 23, 59], RGB-d images [16], images on manifold [60], segmented image decomposition [53], and image registration [15].

To address the unsatisfying artifacts of the TV-norm [13, 67, 55] in the ROF model, much effort is devoted to constructing new regularizers that incorporate higher-order features or nonconvex terms. The Euler’s elastica energy [47, 44, 54, 1]

$$(1.4) \quad \mathcal{R}_{\text{Euler}}(v; a, b) = \int_{\Omega} \left(a + b \left(\nabla \cdot \frac{\nabla v}{|\nabla v|} \right)^2 \right) |\nabla v| d\mathbf{x}$$

has been used for disocclusion [47], inpainting [54], and denoising [1, 63], where $a, b > 0$ are weight parameters. See Figure 1(f) for the reduction of staircase effects by Euler’s elastica. In [43], Lysaker et al. proposed a regularizer based on the Frobenius norm of Hessian:

$$\mathcal{R}_H(v) = \|\partial^2 v\|_{L^1(\Omega)} = \int_{\Omega} \sqrt{v_{xx}^2 + v_{xy}^2 + v_{yx}^2 + v_{yy}^2} d\mathbf{x}.$$

Regarding the image as a manifold in the Euclidean space with higher dimension, Zhu et al. [67] proposed using the L^1 -norm of the mean curvature as the regularizer:

$$\mathcal{R}_{\text{mean}}(v) = \int_{\Omega} \left| \nabla \cdot \left(\frac{\nabla v}{\sqrt{1 + |\nabla v|^2}} \right) \right| d\mathbf{x}.$$

From the same geometric point of view, Liu et al. [40] considered the Gaussian curvature

$$\mathcal{R}_{\text{Gauss}}(v) = \int_{\Omega} \frac{\det \begin{bmatrix} v_{xx} & v_{xy} \\ v_{yx} & v_{yy} \end{bmatrix}}{(1 + |\nabla v|^2)^{3/2}} d\mathbf{x}$$

to reduce image noise while preserving geometric features. Other regularizers substituting the TV-norm include the total generalized variation (TGV) [65, 61], total variation with adaptive exponent [10], nonlocal TV [27], locally modified TV [66], and higher-degree TV [33].

The aforementioned two streams of research focus on improving different parts of the ROF model (1.1), and there are only a few works combining them. In [14], Chan et al. extended [6] by considering the infimum-convolution (inf-convolution) of the TV-norm and the squared L^2 -norm of the Laplacian and arrived at the following model:

$$(1.5) \quad \min_{(v, w, n_1, n_2) \in \text{BV}(\Omega) \times H^2(\Omega) \times G_\mu(\Omega) \times B_{1,1}^1} \left[\int_{\Omega} |\nabla v| + \frac{\alpha}{2} \|\Delta w\|_{L^2(\Omega)}^2 + J^* \left(\frac{n_1}{\mu} \right) + B^* \left(\frac{n_2}{\delta} \right) + \frac{1}{2\lambda} \int_{\Omega} |f - v - w - n_1 - n_2|^2 d\mathbf{x} \right].$$

Here, $\alpha > 0$, $J^*(\frac{n_1}{\mu})$ and $B^*(\frac{n_2}{\delta})$ are the Legendre–Fenchel conjugate of the G -norm and the $B_{-1,\infty}^\infty$ -norm, which enforce boundedness $\|n_1\|_{G(\Omega)} \leq \mu$ and $\|n_2\|_{B_{-1,\infty}^\infty} \leq \delta$, respectively, and $B_{-1,\infty}^\infty$ is the dual to the homogeneous Besov space $B_{1,1}^1$ [46]. In (1.5), v corresponds to the image's piecewise constant part, and w can be associated with the smoothly varying part such as soft lighting and blurry shadows. The n_1 component corresponds to the textures, and the n_2 component captures the noise. Recently, Huska et al. [34] proposed another three-component decomposition model, where a discrete image $f : \Omega \cap \mathbb{N}^2 \rightarrow \mathbb{R}$ is modeled as a sum of a cartoon part v that captures the piecewise constant structures of the image, a smooth part w that models the uneven lighting conditions in the scene, and an oscillatory component n that includes textures and noise. Specifically, their model is

$$(1.6) \quad \min_{v,w,n \in \mathbb{R}^{N \times M}} \left[\beta_1 \|\nabla v\|_0 + \beta_2 \|\partial^2 w\|_2^2 + \beta_3 \|n\|_{H^{-1}(\Omega)}^4 + \frac{1}{2\lambda} \|f - v - w - n\|_2^2 \right],$$

where $\|\nabla v\|_0$ is the discrete L^0 -gradient energy [62] that counts the pixels with nonzero gradient, $\partial^2 w(\mathbf{x}) \in \mathbb{R}^{2 \times 2}$ for each pixel \mathbf{x} is the Hessian matrix, $\|\cdot\|_{H^{-1}(\Omega)}$ is the seminorm of the negative Sobolev space $H^{-1}(\Omega)$ as an approximation of the G -norm, $\|\partial^2 w\|_{L^2(\Omega)}^2 = (\sum_{\mathbf{x} \in \Omega \cap \mathbb{N}^2} w_{xx}^2(\mathbf{x}) + 2w_{xy}^2(\mathbf{x}) + w_{yy}^2(\mathbf{x}))^2$, and β_i , $i = 1, 2, 3$ are positive weight parameters. For numerical computation, they replaced $\|\nabla v\|_0$ by a modified minimax concave (MC) penalty function [64]. Note that the regularization on n is the fourth power of the $H^{-1}(\Omega)$ -seminorm, which was heuristically found to be useful in distinguishing w and n [34]. One of the major drawbacks of solely using the L^0 -gradient regularization is visualized in Figure 1. Since L^0 -gradient regularization is global and heights of boundary jumps do not affect its value, it can lead to strong staircase effects and loss of geometry [13].

In this paper, we propose a new three-component decomposition model to address the issues discussed above. We decompose any grayscale image into its structural part, smooth part, and oscillatory part. For the structural part, our model enforces strong sparsity on the gradient while reducing the presence of staircase effects and encouraging shape-preserving boundary smoothing. We achieve this by proposing a generalized L^0 -gradient energy defined for images over continuous domains and combining it with Euler's elastica (1.4), which controls the magnitude of level-line curvature. For the smooth part, instead of using the Frobenius norm of the Hessian as in (1.6), we substitute it with the squared L^2 -norm of the Laplacian, $\|\Delta w\|_{L^2(\Omega)}^2$, to encourage isotropic smoothness. It can be shown that $\|\Delta w\|_{L^2(\Omega)}^2 = \|\partial^2 w\|_{L^2(\Omega)}^2$ for compactly supported smooth functions [14]; we prove that they have the same critical points under certain boundary conditions (see Appendix B). For the oscillatory part, we use the squared $H^{-1}(\Omega)$ -seminorm as a practical substitute for Meyer's G -norm. It yields not only effective extraction of the oscillations similarly to the 4th power in (1.6), but also significant improvement on the computational efficiency.

Figure 2 illustrates the general performance of our model. The structural part, v^* , contains definite contours and shades with sharp transition; the smooth part, w^* , captures soft intensity variation on the cheeks and chin; and the oscillatory part, n^* , includes noise and textures such as those of the hair. In case the input image does not contain fine-scale textures, the composition $u^* = v^* + w^*$ gives a denoised version of f where the noisy perturbation is removed and sharp boundaries are preserved. The level lines of u^* by our model are more

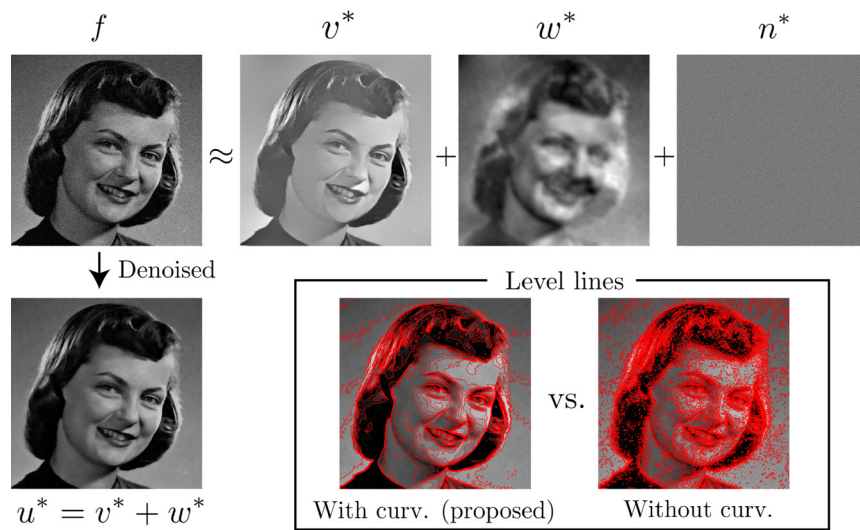


Figure 2. Three-component image decomposition by the proposed method. A grayscale image f is decomposed into a structural part v^* , a smooth part w^* , and an oscillatory part n^* . The sum of v^* and w^* , denoted by u^* , can be regarded as the denoised version of f if the clean image does not have rich textures. Our effectively reduces the staircase effects.

regular compared to those without the curvature regularization. This shows that the proposed model effectively reduces the staircase effects caused by the L^0 -gradient regularization.

Our model involves nonconvex nonsmooth optimization; thus, it is challenging to solve. For the discrete L^0 -gradient minimization, various algorithms and approximations are employed in the literature, such as hard-thresholding [62, 21], region-fusion [48], and penalty approximation [34]. In [49], the L^0 -gradient projection was considered and solved by using a mixed $\ell^{0,1}$ pseudo-norm. Since we introduce a generalized L^0 -gradient energy, a different strategy is taken. Another nontrivial part of our proposed model is the presence of the nonlinear high-order term for the curvatures of level lines. A classical approach is to derive the first variation and then discretize the associated Euler–Lagrange equation [54]. With higher efficiency, various operator-splitting methods (OSMs) and augmented Lagrangian methods (ALMs) [29, 31, 55, 40, 32, 34, 42, 20, 63] have been proposed to handle variational models that contain curvature regularization. OSMs are commonly derived from associating an initial value problem with the formal optimality condition, and ALMs are usually developed via the augmented Lagrangian. These approaches are deeply related and sometimes equivalent [29, 31, 24]. The main advantage of these paradigms come with appropriately splitting the original problem into several subproblems, each of which can be efficiently handled. Recently, connections between OSMs and neural networks are investigated in [35, 56, 39].

To efficiently complete the decomposition, we propose a fast operator-splitting scheme that leverages the fast Fourier transform (FFT) and explicit formulas for the involved subproblems. For an image of size $N \times M$, each iteration of the proposed algorithm has a computational complexity of $\mathcal{O}(MN(\log M + \log N))$. In comparison, the computational complexity in [34] is $\mathcal{O}((MN)^3)$. We present various examples to validate our method. Specifically, we conduct

ablation studies to verify the combination of regularization terms in our method. We design experiments to investigate the impact of regularization parameters. We also demonstrate the effectiveness and efficiency of our approach by comparing it to state-of-the-art models for three-component decomposition.

Our main contributions in this work are the following:

- We propose a new model for decomposing a grayscale image defined on a continuous domain into its structural part, smooth part, and oscillatory part. To achieve satisfying results, we incorporate curvature regularization on level lines along with a sparsity-inducing L^0 -gradient. Our model effectively reduces the undesirable staircase effects and irregular boundary curves caused by the geometry-agnostic L^0 -gradient, yielding more visually appealing components.
- We develop a new operator-splitting scheme to tackle the nonconvex nonsmooth optimization problem associated with our model. The proposed algorithm is computationally efficient. Each subproblem is directly solved or numerically addressed using FFT techniques. Remarkably, when compared to several state-of-the-art methods, our algorithm achieves a speedup of over 10 times.
- We present systematic ablation and comparison studies to justify the effectiveness and efficiency of our proposed method. We also numerically investigate the effects of model parameters and discuss the problem of parameter selection.

The paper is organized as follows. In section 2, we propose our model. In particular, we introduce our model accompanied by mathematical remarks in section 2.1 and reformulate it in section 2.2 for the subsequent algorithmic developments. In section 3, we propose our operator-splitting scheme to address the nonconvex nonsmooth functional minimization problem associated with the reformulated model. In section 4, we describe the discretization and implementation details. In section 5, we present various experiments to justify the proposed model and compare it with other methods from different aspects. We conclude the paper in section 6.

2. Proposed cartoon-smooth-texture decomposition model. In this section, we propose a new model for cartoon-smooth-texture image decomposition integrating Euler's elastica. We present a formal version of our model in section 2.1, where each component is characterized by a functional. Considering the difficulty of the problem, we introduce a reformulation of our model in section 2.1 and derive a formal optimality condition, which paves our way towards developing an efficient operator-splitting scheme in section 3.

2.1. Proposed model. Suppose that $\Omega \subset \mathbb{R}^2$ is a compact domain with a Lipschitz boundary. We assume that a grayscale image $f : \Omega \rightarrow \mathbb{R}$ is a sum of three components with distinctive features. In particular, we consider f to be composed by a structural part $v^* : \Omega \rightarrow \mathbb{R}$ that defines objects with sharp boundaries or regions outlined by strong transitions between the light and the dark; a smooth part $w^* : \Omega \rightarrow \mathbb{R}$ that characterizes the soft intensity variation, such as shadows and uneven lighting; and an oscillatory part $n^* : \Omega \rightarrow \mathbb{R}$ that captures fine-scale textures and noise. Our objective is to extract these three components from f , and we propose to achieve this by considering the following problem:

$$(2.1) \quad \begin{aligned} & \{v^*, w^*, n^*\} \\ & \in \arg \min_{\substack{v, w, n \\ v+w+n=f}} \left[\alpha_0 L_G^0(v) + \alpha_{\text{curv}} \int_{\Omega} \kappa^2(v) |\nabla v| d\mathbf{x} + \alpha_w \|\Delta w\|_{L^2(\Omega)}^2 + \alpha_n \|n\|_{H^{-1}(\Omega)}^2 \right]. \end{aligned}$$

In our proposed model (2.1), each component of the given image f is characterized by different functionals, and we state their mathematical definitions as follows.

- **Structure part v .** Define the function space

$$(2.2) \quad \begin{aligned} \mathcal{V}(\Omega) = \left\{ v \in H^1(\Omega) \mid \boldsymbol{\nu}_v \in H(\text{div}, \Omega), \right. \\ \left. \text{where, for } \mathbf{x} \in \Omega, \boldsymbol{\nu}_v(\mathbf{x}) = \frac{\nabla v(\mathbf{x})}{|\nabla v(\mathbf{x})|} \text{ if } |\nabla v(\mathbf{x})| \neq 0 \text{ and } \mathbf{0}, \text{ otherwise} \right\}, \end{aligned}$$

and $H(\text{div}, \Omega)$ denotes the Hilbert space of square-integrable vector fields on Ω with square-integrable weak divergences; see, for example, [3]. In this work, we define the L^0 -gradient energy of $v \in \mathcal{V}(\Omega)$ as

$$(2.3) \quad L_G^0(v) = \int_{\Omega} \mathbb{H}(|\nabla v|) d\mathbf{x},$$

where $\mathbb{H}(\cdot)$ denotes the Heaviside step function, which outputs a value of 1 for positive inputs and a value of 0, otherwise.

Moreover, since $v \in \mathcal{V}(\Omega)$, we can interpret the Euler's elastica part as

$$(2.4) \quad \int_{\Omega} \kappa^2(v) |\nabla v| d\mathbf{x} = \int_{\Omega} |\nabla \cdot \boldsymbol{\nu}_v|^2 |\nabla v| d\mathbf{x},$$

where $\boldsymbol{\nu}_v$ is defined as in (2.2) and $\nabla \cdot \boldsymbol{\nu}_v$ denotes its weak divergence. By the definition of $\mathcal{V}(\Omega)$, (2.4) is finite and well-defined.

- **Smooth part w .** We take $w \in H^2(\Omega)$ and define

$$(2.5) \quad \|\Delta w\|_{L^2(\Omega)}^2 = \int_{\Omega} (\partial_x^2 w(\mathbf{x}) + \partial_y^2 w(\mathbf{x}))^2 d\mathbf{x}.$$

Here, the partial derivatives ∂_x^2 and ∂_y^2 are understood in the weak sense. Its effect is similar to that of the squared L^2 -norm of the second-order derivatives, i.e., $\|\partial^2 w\|_{L^2(\Omega)}^2$ used in (1.6). Under certain boundary conditions, we show that they are equivalent in the sense of having the same critical points (see Appendix B), which generalizes the observation in [14]. Using this term, we gain significant computational efficiency thanks to the simpler first variation (see section 3).

- **Oscillatory part w .** As for the oscillatory part, we take $n \in H^{-1}(\Omega)$ and use the squared inverse Sobolev norm

$$(2.6) \quad \|n\|_{H^{-1}(\Omega)}^2 = \|\nabla \Delta^{-1} n\|_{L^2(\Omega)}^2$$

as a practical approximation for Meyer's G -norm.

We design functionals in (2.1) for better visual effects and computational efficiency. The sparsity-inducing L^0 -gradient energy (2.3) punishes nonzero gradients independent of their magnitudes, yielding results with higher contrast; this also implies stronger staircasing effects. To reduce such artifacts in v , our second term regularizes the TV-weighted squared curvatures of its level lines. It combines high-order derivative information of the image, which has been shown to be an effective strategy for improving the visual effects of the reconstruction [14]. The squared L^2 -norm of the Laplacian encourages isotropic smoothness of w , modeling the gradual changes of illumination over the scene. The inverse Sobolev norm on the oscillatory component was discussed in [46, 50, 34].

Remark 2.1. We note that (2.3) is a continuous analogue of the discrete L^0 -gradient energy [62, 34]. In particular, for a discrete image $v_D : \Omega \times \mathbb{N}^2 \rightarrow \mathbb{R}$, we can obtain a continuous extension $v : \Omega \rightarrow \mathbb{R}$ by bilinear interpolation; then, $v \in \mathcal{V}(\Omega)$ and $\|\nabla v_D\|_0$ equals $L_G^0(v)$ multiplied by a constant factor. It is possible to consider more general function spaces for the structure part, e.g., the space of bounded variation functions $BV(\Omega)$ or de Giorgi and Ambrosio's $SBV(\Omega)$ [19], and the L^0 -gradient energy may be defined via mollification. An alternative is to consider a sufficiently smooth approximation such as the MC penalty function [64, 34]. For the Euler's elastica part, the major technical problem is that level lines of BV functions generally lack the sufficient regularity to define curvature in the classical sense. One strategy is to restrict v to $C^2(\Omega)$ [45]; another approach is to define the weak curvature for BV functions after mollification [54]; a different paradigm involves considering the solution of the p -Laplacian equation as $p \rightarrow 1^+$; yet another method relies on the pairing theory [2] for distributions [51]. In our setting, although v needs to be continuous in theory, it does not cause practical problems by our splitting algorithm (see section 3). We shall leave the challenging study on generalizations in the future works.

Remark 2.2. No matter which mathematical definitions are used for interpretation, our model (2.1) is challenging to analyze for the existence of minimizers. The main difficulty is caused by the L^0 -gradient energy and the Euler's elastica energy. If we use the TV-norm for regularizing v instead, the resulting model becomes convex, and the existence property can be derived similarly to [14]. With an additional restriction on the mean value of w , then the uniqueness can be established. If we replace the L^0 -gradient energy by the TV-norm, we recover the ordinary Euler's elastica [44, 45, 54] for the v component, and the related analysis on semicontinuity in the context of Γ -convergence can be found in [9].

Remark 2.3. In our proposed model (2.1), both the regularization on the curvature of level lines of v^* and the regularization on the Laplacian of w^* encourage smoothness. However, they emphasize different types of smoothing. The curvature regularization on v^* admits a geometric prior that prefers straight level lines, whereas the regularization on w^* has no preferences in diffusion directions; i.e., it is isotropic.

There exist functions w defined on $\Omega \subset \mathbb{R}^2$ whose curvatures of level lines are constantly zero, but not harmonic. For example, consider $w(x_1, x_2) = x_1^2$ defined over $(x_1, x_2) \in \Omega = [-1, 1] \times [-1, 1]$. There also exist harmonic functions whose level lines have nonzero curvatures, such as $v(x_1, x_2) = x_1^2 - x_2^2$. For general images, the amount of smoothness in a given image can be transferred between v^* and w^* depending on the ratio $\alpha_{\text{curv}}/\alpha_w$. We investigate this special property of our model in section 5 using real images.

We emphasize that the v^* component is also regularized by (2.3), which is crucial in distinguishing the structural features in v^* from the soft shading and blurry shapes represented by w^* . Consider a Gaussian blurred smooth function $f_\varepsilon(x_1, x_2) = G_\varepsilon * h(x_1, x_2)$ defined on $[0, 1] \times [0, 1]$, where $h(x_1, x_2) = 1$ if $0 \leq x_1 \leq 0.5, 0 \leq x_2 \leq 1$ and $h(x_1, x_2) = 0$, otherwise; G_ε is the Gaussian kernel with standard deviation $\varepsilon > 0$; and $*$ is the convolution. The level lines of f_ε remain straight, and $\|\Delta f\|_{L^2(\Omega)}^2 = \mathcal{O}(\varepsilon^{-4}) > 0$, which decreases in ε . If v^* is only penalized by the curvature of its level line and we ignore the oscillatory component for simplicity, then the optimal decomposition is $v^* = f_\varepsilon$ and $w^* = 0$ for any choice of ε . This is contradictory to the visual perception of homogeneous structures with clear boundaries. To consider the L^0 -gradient, we first note that the Gaussian kernel has a compact support in the discrete sense. In particular, for a fixed threshold $\gamma > 0$, we note that

$$\frac{1}{\varepsilon\sqrt{2\pi}} \exp\left(-\frac{x_1^2}{2\varepsilon^2}\right) > \gamma$$

only if

$$-\sqrt{-2\varepsilon^2 \ln(\gamma\varepsilon\sqrt{2\pi})} \leq x_1 \leq \sqrt{-2\varepsilon^2 \ln(\gamma\varepsilon\sqrt{2\pi})}.$$

Hence, $L_G^0(f_\varepsilon) \approx 2\sqrt{-2\varepsilon^2 \ln(\gamma\varepsilon\sqrt{2\pi})}$, which increases when ε is bigger; i.e., f_ε is blurrier. With appropriate choices of the parameter α_0 and α_n , the optimal decomposition will be $v^* = 0$ and $w^* = f_\varepsilon$ if ε is sufficiently large, and the optimal decomposition becomes $v^* = f_\varepsilon$ and $w^* = 0$ if ε is sufficiently small. By considering the L^0 -gradient of v^* component, the decomposition is compatible with visual perception.

2.2. Model reformulation and formal optimality condition. As discussed above, the model (2.1) is nontrivial to analyze and solve. To arrive at a practical form that can be numerically addressed, we relax (2.1) by rewriting the constraint $f = v + w + n$ as a quadratic penalization. Our modified model is

$$(2.7) \quad \min_{\substack{v \in \mathcal{V}(\Omega), \\ w \in H^2(\Omega), n \in H^{-1}(\Omega)}} \left[\alpha_0 \int_{\Omega} \mathbb{H}(|\nabla v|) d\mathbf{x} + \alpha_{\text{curv}} \int_{\Omega} |\nabla \cdot \boldsymbol{\nu}_v|^2 |\nabla v| d\mathbf{x} + \alpha_w \|\Delta w\|_{L^2(\Omega)}^2 + \alpha_n \|n\|_{H^{-1}(\Omega)}^2 + \frac{1}{2} \|f - (v + w + n)\|_{L^2(\Omega)}^2 \right],$$

where v, w , and n stand for the same components as in (2.1) and $\mathcal{V}(\Omega)$ is defined in (2.2). We then resolve the high-order and nonlinear term associated with the curvature by introducing auxiliary variables $\mathbf{q}(\mathbf{x}) = \nabla v(\mathbf{x})$ and $\boldsymbol{\mu}(\mathbf{x}) = \mathbf{q}(\mathbf{x})/|\mathbf{q}(\mathbf{x})|$, which satisfy the obvious constraints $\mathbf{q}(\mathbf{x}) \cdot \boldsymbol{\mu}(\mathbf{x}) = |\mathbf{q}(\mathbf{x})|$ and $|\boldsymbol{\mu}(\mathbf{x})| \leq 1$ for any $\mathbf{x} \in \Omega$, as in [20]. Moreover, if we let $\mathbf{g} = (g_1, g_2) = \nabla \Delta^{-1} v \in L^2(\Omega) \times L^2(\Omega)$ as in [50], then (2.7) is rewritten as

$$(2.8) \quad \begin{cases} \min_{\substack{v \in H^1(\Omega) \\ \mathbf{q} \in (L^2(\Omega))^2, \mu \in (H^1(\Omega))^2 \\ w \in H^2(\Omega), \mathbf{g} \in (H^1(\Omega))^2}} & \left[\alpha_0 \int_{\Omega} \mathbb{H}(|\mathbf{q}|) d\mathbf{x} + \alpha_{\text{curv}} \int_{\Omega} (\nabla \cdot \boldsymbol{\mu})^2 |\mathbf{q}| d\mathbf{x} \right. \\ & \left. + \alpha_w \|\Delta w\|_{L^2(\Omega)}^2 + \alpha_n \|\mathbf{g}\|_{L^2(\Omega)}^2 + \frac{1}{2} \|f - (v + w + \nabla \cdot \mathbf{g})\|_{L^2(\Omega)}^2 \right] \\ \mathbf{q} = \nabla v, \\ \boldsymbol{\mu} = \frac{\mathbf{q}}{|\mathbf{q}|}, \\ |\boldsymbol{\mu}| \leq 1. \end{cases}$$

We note that model (2.8) can be further simplified by observing the following characterization of minimizers of model (2.7), whose proof is in Appendix A.

Proposition 2.1. *Let (v^*, w^*, n^*) be a minimizer of (2.7); then, we have that*

$$(2.9) \quad \int_{\Omega} v^* + w^* + n^* d\mathbf{x} = \int_{\Omega} f d\mathbf{x}.$$

Proposition 2.1 is a consequence of L^2 minimization, which has been used in the literature; see [20], for example. This implies that, if $(v^*, \mathbf{q}^*, \boldsymbol{\mu}^*, w^*, \mathbf{g}^*)$ is a minimizer of model (2.8), v^* solves the Poisson equation

$$(2.10) \quad \begin{cases} \Delta v = \nabla \cdot \mathbf{q}^* & \text{in } \Omega, \\ (\nabla v - \mathbf{q}^*) \cdot \mathbf{n} = 0 & \text{on } \partial\Omega, \\ \int_{\Omega} v d\mathbf{x} = \int_{\Omega} f - w^* - \nabla \cdot \mathbf{g}^* d\mathbf{x}, \end{cases}$$

where \mathbf{n} denotes the outward normal direction along $\partial\Omega$. Since the condition $\int_{\Omega} \nabla \cdot \mathbf{q}^* d\mathbf{x} = \int_{\partial\Omega} \mathbf{q}^* \cdot \mathbf{n} d\sigma(\mathbf{x})$ follows from the divergence theorem, where $\sigma(\cdot)$ is the surface measure, (2.10) admits a unique solution [25]. This fact allows us to express v via \mathbf{q} , w , and \mathbf{g} , thus reducing the number of optimizing variables by one.

It is difficult to directly optimize the L^0 -gradient energy since the integrand inside the integral is discontinuous. To bypass this difficulty during the derivation of our algorithm, we consider a smoothed version

$$(2.11) \quad \mathcal{R}_a(\mathbf{p}) = \int_{\Omega} \frac{a|\mathbf{p}|}{1+a|\mathbf{p}|} d\mathbf{x}, \quad a > 0.$$

When a is finite, $\mathcal{R}_a(\cdot)$ is locally Lipschitzian; moreover, we have that

$$\lim_{a \rightarrow +\infty} \mathcal{R}_a(\mathbf{q}) = \int_{\Omega} \mathbb{H}(|\mathbf{q}|) d\mathbf{x}.$$

Utilizing (2.10) and (2.11), we consider an approximation of (2.8) as

$$(2.12) \quad \begin{aligned} \min_{\substack{\mathbf{q} \in (L^2(\Omega))^2, \boldsymbol{\mu} \in (H^1(\Omega))^2 \\ w \in H^2(\Omega), \mathbf{g} \in (H^1(\Omega))^2}} & \left[\alpha_0 \mathcal{R}_a(\mathbf{q}) + \alpha_{\text{curv}} \int_{\Omega} |\nabla \cdot \boldsymbol{\mu}|^2 |\mathbf{q}| d\mathbf{x} + \alpha_w \int_{\Omega} |\Delta w|^2 d\mathbf{x} \right. \\ & \left. + \alpha_n \int_{\Omega} |\mathbf{g}|^2 d\mathbf{x} + \frac{1}{2} \int_{\Omega} |f - (v_{\mathbf{q}, w, \mathbf{g}} + w + \nabla \cdot \mathbf{g})|^2 d\mathbf{x} + I_{\Sigma_f}(\mathbf{q}, w, \mathbf{g}) + I_S(\mathbf{q}, \boldsymbol{\mu}) \right], \end{aligned}$$

where $v_{\mathbf{q}, w, \mathbf{g}}$ is uniquely determined by $\mathbf{q}, w, \mathbf{g}$ via (2.10) and the indicator functions

$$I_{\Sigma_f}(\mathbf{q}, w, \mathbf{g}) = \begin{cases} 0 & \text{if } (\mathbf{q}, w, \mathbf{g}) \in \Sigma_f, \\ +\infty, & \text{otherwise,} \end{cases} \quad I_S(\mathbf{q}, \boldsymbol{\mu}) = \begin{cases} 0 & \text{if } (\mathbf{q}, \boldsymbol{\mu}) \in S, \\ +\infty, & \text{otherwise} \end{cases}$$

with

$$\begin{aligned} \Sigma_f = & \left\{ (\mathbf{q}, w, \mathbf{g}) \in (L^2(\Omega))^2 \times L^2(\Omega) \times (H^1(\Omega))^2 \mid \right. \\ & \exists v \in H^1(\Omega) \text{ such that } \mathbf{q} = \nabla v \text{ and } \int_{\Omega} (v + w + \nabla \cdot \mathbf{g} - f) d\mathbf{x} = 0 \Big\}, \\ S = & \{(\mathbf{q}, \boldsymbol{\mu}) \in (L^2(\Omega))^2 \times (L^2(\Omega))^2 \mid \mathbf{q} \cdot \boldsymbol{\mu} = |\mathbf{q}|, |\boldsymbol{\mu}| \leq 1\}. \end{aligned}$$

Assuming that (2.12) has a minimizer $\{\mathbf{q}^*, \boldsymbol{\mu}^*, w^*, \mathbf{g}^*\}$ (see Remark 2.4), we have that $v^* = v_{\mathbf{q}^*, w^*, \mathbf{g}^*}$ for the structural part, w^* for the smooth part, and $n^* = \nabla \cdot \mathbf{g}^*$ for the oscillatory part. Moreover, we denote

$$\begin{aligned} J_0(\mathbf{q}, w, \mathbf{g}) &= \frac{1}{2} \int_{\Omega} |f - (v_{\mathbf{q}, w, \mathbf{g}} + w + \nabla \cdot \mathbf{g})|^2 d\mathbf{x}, \\ J_1(\mathbf{q}) &= \alpha_0 \mathcal{R}_a(\mathbf{q}), \\ J_2(\mathbf{q}, \boldsymbol{\mu}) &= \alpha_{\text{curv}} \int_{\Omega} |\nabla \cdot \boldsymbol{\mu}|^2 |\mathbf{q}| d\mathbf{x}, \\ J_3(w) &= \alpha_w \int_{\Omega} |\Delta w|^2 d\mathbf{x}, \\ J_4(\mathbf{g}) &= \alpha_n \int_{\Omega} |\mathbf{g}|^2 d\mathbf{x}, \end{aligned}$$

and the minimizer $\{\mathbf{q}^*, \boldsymbol{\mu}^*, w^*, \mathbf{g}^*\}$ satisfies the formal optimality condition

(2.13)

$$\begin{cases} \partial_{\mathbf{q}} J_1(\mathbf{q}^*) + \partial_{\mathbf{q}} J_2(\mathbf{q}^*, \boldsymbol{\mu}^*) + \partial_{\mathbf{q}} J_0(\mathbf{q}^*, w^*, \mathbf{g}^*) + \partial_{\mathbf{q}} I_{\Sigma_f}(\mathbf{q}^*, w^*, \mathbf{g}^*) + \partial_{\mathbf{q}} I_S(\mathbf{q}^*, \boldsymbol{\mu}^*) \ni 0, \\ \partial_{\boldsymbol{\mu}} J_2(\mathbf{q}^*, \boldsymbol{\mu}^*) + \partial_{\boldsymbol{\mu}} I_S(\mathbf{q}^*, \boldsymbol{\mu}^*) \ni 0, \\ \partial_w J_3(w^*) + \partial_w J_0(\mathbf{q}^*, w^*, \mathbf{g}^*) + \partial_w I_{\Sigma_f}(\mathbf{q}^*, w^*, \mathbf{g}^*) \ni 0, \\ \partial_{\mathbf{g}} J_4(\mathbf{g}^*) + \partial_{\mathbf{g}} J_0(\mathbf{q}^*, w^*, \mathbf{g}^*) + \partial_{\mathbf{g}} I_{\Sigma_f}(\mathbf{q}^*, w^*, \mathbf{g}^*) \ni 0, \end{cases}$$

where ∂ is the generalized gradient [18, section 1.2, equation (2)] extended to functionals.

Remark 2.4. The existence of a minimizer for (2.12) can ensure the validity of (2.13). Indeed, (2.13) involves locally Lipschitz functions and indicator functionals. According to [18, Proposition 2.3.3], the generalized gradient of the sum of functions is a subset of the sum of the generalized gradient of each function, which can be also extended to indicator functionals. In this paper, we focus on the algorithmic development, leaving the question of existence to future research.

3. Operator-splitting algorithm for the proposed model. In this section, we propose an efficient algorithm for model (2.12) based on an operator-splitting framework. In section 2.2, we associate the model with a gradient flow based on its formal optimality condition. In section 3.1, we present a novel operator-splitting scheme to solve the reformulated model. This nonconvex nonsmooth minimization problem is decomposed into several subproblems, whose

Table 1
Notation of general variables and PDE solutions and their correspondences.

	Correspondence			
General variables	\mathbf{q}	μ	w	\mathbf{g}
PDE solutions	\mathbf{p}	$\boldsymbol{\lambda}$	r	\mathbf{s}

solutions are described in sections 3.2–3.4. In section 3.5, we adapt the proposed algorithm to the periodic boundary condition. We summarize the proposed scheme in Algorithm 3.1.

3.1. Proposed scheme. We associate (2.13) with the following initial value problem analogously to the gradient flow:

$$(3.1) \quad \begin{cases} \frac{\partial \mathbf{p}}{\partial t} + \partial_{\mathbf{q}} J_1(\mathbf{p}) + \partial_{\mathbf{q}} J_2(\mathbf{p}, \boldsymbol{\lambda}) + \partial_{\mathbf{q}} J_0(\mathbf{p}, r, \mathbf{s}) + \partial_{\mathbf{q}} I_{\Sigma_f}(\mathbf{p}) + \partial_{\mathbf{q}} I_S(\mathbf{p}, \boldsymbol{\lambda}) \ni 0, \\ \gamma_1 \frac{\partial \boldsymbol{\lambda}}{\partial t} + \partial_{\boldsymbol{\mu}} J_2(\mathbf{p}, \boldsymbol{\lambda}) + \partial_{\boldsymbol{\mu}} I_S(\mathbf{p}, \boldsymbol{\lambda}) \ni 0, \\ \gamma_2 \frac{\partial r}{\partial t} + \partial_w J_3(r) + \partial_w J_0(\mathbf{p}, r, \mathbf{s}) = 0, \\ \gamma_3 \frac{\partial \mathbf{s}}{\partial t} + \partial_{\mathbf{g}} J_4(\mathbf{s}) + \partial_{\mathbf{g}} J_0(\mathbf{p}, w, \mathbf{s}) = 0, \\ \{\mathbf{p}(0), \boldsymbol{\lambda}(0), r(0), \mathbf{s}(0)\} = \{\mathbf{p}_0, \boldsymbol{\lambda}_0, r_0, \mathbf{s}_0\}, \end{cases}$$

where $\{\mathbf{p}_0, \boldsymbol{\lambda}_0, r_0, \mathbf{s}_0\}$ is a given initial condition and $\gamma_1, \gamma_2, \gamma_3 > 0$ are parameters that control the evolution speed of $\mathbf{p}, \boldsymbol{\lambda}, r, \mathbf{s}$, respectively. We note that the steady state solution of (3.1) satisfies the optimality condition (2.13) for model (2.12). To avoid confusion, we distinguish the time-dependent variables in (3.1) from the optimization variables in (2.12), and Table 1 shows the correspondences.

We find the steady state solution of (3.1) by employing the operator-splitting framework [31, 30]. Our proposed scheme proceeds as follows.

Initialization

$$\text{Initialize } \{\mathbf{p}^0, \boldsymbol{\lambda}^0, r^0, \mathbf{s}^0\} = \{\mathbf{p}_0, \boldsymbol{\lambda}_0, r_0, \mathbf{s}_0\}.$$

Fix some $\tau > 0$ as the time step. For $k = 0, 1, 2, \dots$, denote $t^k = k\tau$ for $k = 0, 1, 2, \dots$, and we update $\{\mathbf{p}^k, \boldsymbol{\lambda}^k, r^k, \mathbf{s}^k\} \rightarrow \{\mathbf{p}^{k+1}, \boldsymbol{\lambda}^{k+1}, r^{k+1}, \mathbf{s}^{k+1}\}$ via four fractional steps.

Fractional step 1: Solve

$$\begin{cases} \frac{\partial \mathbf{p}}{\partial t} + \partial_{\mathbf{q}} J_1(\mathbf{p}) \ni 0, \\ \gamma_1 \frac{\partial \boldsymbol{\lambda}}{\partial t} = 0, \\ \gamma_2 \frac{\partial r}{\partial t} = 0, \\ \gamma_3 \frac{\partial \mathbf{s}}{\partial t} = 0 \\ \{\mathbf{p}(t^k), \boldsymbol{\lambda}(t^k), r(t^k), \mathbf{s}(t^k)\} = \{\mathbf{p}^k, \boldsymbol{\lambda}^k, r^k, \mathbf{s}^k\}, \end{cases} \quad \text{in } \Omega \times (t^k, t^{k+1}),$$

and set

$$\{\mathbf{p}^{k+1/4}, \boldsymbol{\lambda}^{k+1/4}, r^{k+1/4}, \mathbf{s}^{k+1/4}\} = \{\mathbf{p}(t^{k+1}), \boldsymbol{\lambda}(t^{k+1}), r(t^{k+1}), \mathbf{s}(t^{k+1})\}.$$

Fractional step 2: Solve

$$\begin{cases} \frac{\partial \mathbf{p}}{\partial t} + \partial_{\mathbf{q}} J_2(\mathbf{p}, \boldsymbol{\lambda}) = 0, \\ \gamma_1 \frac{\partial \boldsymbol{\lambda}}{\partial t} + \partial_{\boldsymbol{\mu}} J_2(\mathbf{p}, \boldsymbol{\lambda}) \ni 0, \\ \gamma_2 \frac{\partial r}{\partial t} = 0, \\ \gamma_3 \frac{\partial \mathbf{s}}{\partial t} = 0 \\ \{\mathbf{p}(t^k), \boldsymbol{\lambda}(t^k), r(t^k), \mathbf{s}(t^k)\} = \{\mathbf{p}^{k+1/4}, \boldsymbol{\lambda}^{k+1/4}, r^{k+1/4}, \mathbf{s}^{k+1/4}\}, \end{cases} \quad \text{in } \Omega \times (t^k, t^{k+1}),$$

and set

$$\{\mathbf{p}^{k+2/4}, \boldsymbol{\lambda}^{k+2/4}, r^{k+2/4}, \mathbf{s}^{k+2/4}\} = \{\mathbf{p}(t^{k+1}), \boldsymbol{\lambda}(t^{k+1}), r(t^{k+1}), \mathbf{s}(t^{k+1})\}.$$

Fractional step 3: Solve

$$\begin{cases} \frac{\partial \mathbf{p}}{\partial t} + \partial_{\mathbf{q}} I_S(\mathbf{p}, \boldsymbol{\lambda}) \ni 0, \\ \gamma_1 \frac{\partial \boldsymbol{\lambda}}{\partial t} + \partial_{\boldsymbol{\mu}} I_S(\mathbf{p}, \boldsymbol{\lambda}) \ni 0, \\ \gamma_2 \frac{\partial r}{\partial t} = 0, \\ \gamma_3 \frac{\partial \mathbf{s}}{\partial t} = 0 \\ \{\mathbf{p}(t^k), \boldsymbol{\lambda}(t^k), r(t^k), \mathbf{s}(t^k)\} = \{\mathbf{p}^{k+2/4}, \boldsymbol{\lambda}^{k+2/4}, r^{k+2/4}, \mathbf{s}^{k+2/4}\}, \end{cases} \quad \text{in } \Omega \times (t^k, t^{k+1}),$$

and set

$$\{\mathbf{p}^{k+3/4}, \boldsymbol{\lambda}^{k+3/4}, r^{k+3/4}, \mathbf{s}^{k+3/4}\} = \{\mathbf{p}(t^{k+1}), \boldsymbol{\lambda}(t^{k+1}), r(t^{k+1}), \mathbf{s}(t^{k+1})\}.$$

Fractional step 4: Solve

$$\begin{cases} \frac{\partial \mathbf{p}}{\partial t} + \partial_{\mathbf{q}} J_0(\mathbf{p}, r, \mathbf{s}) + \partial_{\mathbf{q}} I_{\Sigma_f}(\mathbf{p}, r, \mathbf{s}) \ni 0, \\ \gamma_1 \frac{\partial \boldsymbol{\lambda}}{\partial t} = 0, \\ \gamma_2 \frac{\partial r}{\partial t} + \partial_w J_0(\mathbf{p}, r, \mathbf{s}) + \partial_w J_3(r) + \partial_w I_{\Sigma_f}(\mathbf{p}, r, \mathbf{s}) \ni 0, \\ \gamma_3 \frac{\partial \mathbf{s}}{\partial t} + \partial_{\mathbf{g}} J_0(\mathbf{p}, r, \mathbf{s}) + \partial_{\mathbf{g}} J_4(\mathbf{s}) + \partial_{\mathbf{g}} I_{\Sigma_f}(\mathbf{p}, r, \mathbf{s}) \ni 0 \\ \{\mathbf{p}(t^k), \boldsymbol{\lambda}(t^k), r(t^k), \mathbf{s}(t^k)\} = \{\mathbf{p}^{k+3/4}, \boldsymbol{\lambda}^{k+3/4}, r^{k+3/4}, \mathbf{s}^{k+3/4}\}, \end{cases} \quad \text{in } \Omega \times (t^k, t^{k+1}),$$

and set

$$\{\mathbf{p}^{k+1}, \boldsymbol{\lambda}^{k+1}, r^{k+1}, \mathbf{s}^{k+1}\} = \{\mathbf{p}(t^{k+1}), \boldsymbol{\lambda}(t^{k+1}), r(t^{k+1}), \mathbf{s}(t^{k+1})\}.$$

We time discretize the systems above by the Marchuk–Yanenko scheme and get

$$(3.2) \quad \begin{cases} \frac{\mathbf{p}^{k+1/4} - \mathbf{p}^k}{\tau} + \partial_{\mathbf{q}} J_1(\mathbf{p}^{k+1/4}) \ni 0, \\ \gamma_1 \frac{\boldsymbol{\lambda}^{k+1/4} - \boldsymbol{\lambda}^k}{\tau} = 0, \\ \gamma_2 \frac{r^{k+1/4} - r^k}{\tau} = 0, \\ \gamma_3 \frac{s^{k+1/4} - s^k}{\tau} = 0, \end{cases}$$

$$(3.3) \quad \begin{cases} \frac{\mathbf{p}^{k+2/4} - \mathbf{p}^{k+1/4}}{\tau} + \partial_{\mathbf{q}} J_2(\mathbf{p}^{k+2/4}, \boldsymbol{\lambda}^{k+1/4}) \ni 0, \\ \gamma_1 \frac{\boldsymbol{\lambda}^{k+2/4} - \boldsymbol{\lambda}^{k+1/4}}{\tau} + \partial_{\mu} J_2(\mathbf{p}^{k+2/4}, \boldsymbol{\lambda}^{k+2/4}) \ni 0, \\ \gamma_2 \frac{r^{k+2/4} - r^{k+1/4}}{\tau} = 0, \\ \gamma_3 \frac{s^{k+2/4} - s^{k+1/4}}{\tau} = 0, \end{cases}$$

$$(3.4) \quad \begin{cases} \frac{\mathbf{p}^{k+3/4} - \mathbf{p}^{k+2/4}}{\tau} + \partial_{\mathbf{q}} I_S(\mathbf{p}^{k+3/4}, \boldsymbol{\lambda}^{k+3/4}) \ni 0, \\ \gamma_1 \frac{\boldsymbol{\lambda}^{k+3/4} - \boldsymbol{\lambda}^{k+2/4}}{\tau} + \partial_{\mu} I_S(\mathbf{p}^{k+3/4}, \boldsymbol{\lambda}^{k+3/4}) \ni 0, \\ \gamma_2 \frac{r^{k+3/4} - r^{k+2/4}}{\tau} = 0, \\ \gamma_3 \frac{s^{k+3/4} - s^{k+2/4}}{\tau} = 0, \end{cases}$$

$$(3.5) \quad \begin{cases} \frac{\mathbf{p}^{k+1} - \mathbf{p}^{k+3/4}}{\tau} + \partial_{\mathbf{q}} J_0(\mathbf{p}^{k+1}, r^{k+1}, \mathbf{s}^{k+1}) + \partial_{\mathbf{q}} I_{\Sigma_f}(\mathbf{p}^{k+1}, r^{k+1}, \mathbf{s}^{k+1}) \ni 0, \\ \gamma_1 \frac{\boldsymbol{\lambda}^{k+1} - \boldsymbol{\lambda}^{k+3/4}}{\tau} = 0, \\ \gamma_2 \frac{r^{k+1} - r^{k+3/4}}{\tau} + \partial_w J_0(\mathbf{p}^{k+1}, r^{k+1}, \mathbf{s}^{k+1}) + \partial_w J_3(r^{k+1}) + \partial_w I_{\Sigma_f}(\mathbf{p}^{k+1}, r^{k+1}, \mathbf{s}^{k+1}) \ni 0, \\ \gamma_3 \frac{\mathbf{s}^{k+1} - \mathbf{s}^{k+3/4}}{\tau} + \partial_{\mathbf{g}} J_0(\mathbf{p}^{k+1}, r^{k+1}, \mathbf{s}^{k+1}) + \partial_{\mathbf{g}} J_4(\mathbf{s}^{k+1}) + \partial_{\mathbf{g}} I_{\Sigma_f}(\mathbf{p}^{k+1}, r^{k+1}, \mathbf{s}^{k+1}) \ni 0 \end{cases}$$

for $k = 0, 1, 2, \dots$. We note that each system above corresponds to a subproblem that can be solved explicitly or approximated efficiently. In the following sections, we describe the details.

Remark 3.1. Scheme (3.2)–(3.5) is an approximation of the gradient flow. Its convergence closely relates to that of the gradient flow together with an approximation error. It is shown that, when there is only one variable and the operators in each step are smooth enough, the approximation error is on the order of $O(\tau)$ (see [17] and [28, Chapter 6]). In this article, due to the complicated structures of J_1, J_2, I_{Σ_f} , and I_S , we cannot use existing tools to analyze the convergence rate and need to study it separately.

3.2. On the solution to subproblem (3.2) and (3.3). Given \mathbf{p}^k for $k = 0, 1, 2, \dots$, the vector field $\mathbf{p}^{k+1/4}$ solves

$$\mathbf{p}^{k+1/4} = \arg \min_{\mathbf{q} \in (L^2(\Omega))^2} \left[\frac{1}{2} \int_{\Omega} |\mathbf{q} - \mathbf{p}^k|^2 dx + \tau \alpha_0 \mathcal{R}_a(\mathbf{q}) \right].$$

It can be checked that, when $\mathbf{p}^k(\mathbf{x}) = \mathbf{0}$, $\mathbf{p}^{k+1/4}(\mathbf{x}) = \mathbf{0}$, and when $\mathbf{p}^k(\mathbf{x}) \neq \mathbf{0}$, then either $\mathbf{p}^{k+1/4} = \mathbf{0}$ or $\mathbf{p}^{k+1/4}(\mathbf{x})$ is a nonzero vector satisfying

$$(3.6) \quad \left(|\mathbf{p}^{k+1/4}(\mathbf{x})| + \frac{\tau \alpha_0 a}{(1 + a|\mathbf{p}^{k+1/4}(\mathbf{x})|)^2} \right) \frac{\mathbf{p}^{k+1/4}(\mathbf{x})}{|\mathbf{p}^{k+1/4}(\mathbf{x})|} = \mathbf{p}^k(\mathbf{x}).$$

Denote $p^k = |\mathbf{p}^k(\mathbf{x})|$, and define

$$(3.7) \quad g_a^k(y) = a^2 y^3 + a(2 - ap^k)y^2 + (1 - 2ap^k)y - p^k + a\tau\alpha_0;$$

then, (3.6) implies that $|\mathbf{p}^{k+1}(\mathbf{x})|$ is a positive root of (3.7). Since the differential of g_a^k has roots $y_1 = -a^{-1}$ and $y_2 = (3a)^{-1}(2ap^k - 1)$ with $y_1 < y_2$, $g_a^k(y)$ is strictly increasing for $y \in (-\infty, y_1) \cup (y_2, +\infty)$ and strictly decreasing for $y \in (y_1, y_2)$. Now, we consider two cases:

- If $p^k \leq (2a)^{-1}$, then, since $g_a^k(0) = a\tau\alpha_0 - p^k$, g_a^k has a positive root when $a\tau\alpha_0 < p^k \leq (2a)^{-1}$ and does not have any positive root when $p^k \leq a\tau\alpha_0$.
- If $p^k > (2a)^{-1}$, g_a^k has at least one positive root if and only if $g_a^k(y_2) < 0$, which requires that

$$u^k(p^k) := 4a^3(p^k)^3 + 3a^2(4(p^k)^2 - 9\tau\alpha_0) + 12ap^k + 4 > 0,$$

and this holds if $p^k > p^* := 3(\tau\alpha_0/4a)^{1/3} - a^{-1}$. If we set τ such that $2\tau\alpha_0 < a^{-2}$, then $(2a)^{-1} > p^*$ and $u^k((2a)^{-1}) = 27(1/2 - a^2\tau\alpha_0) > 0$; hence, (3.7) always has a positive root when $2\tau\alpha_0 < a^{-2}$.

In summary, if $2\tau\alpha_0 < a^{-2}$ and $p^k > (\tau\alpha_0/2)^{1/2}$, (3.6) has at least one solution. Note that (3.6) indicates that $\mathbf{p}^{k+1/4}(\mathbf{x})$ and $\mathbf{p}^k(\mathbf{x})$ have the same direction and that $|\mathbf{p}^k(\mathbf{x})| = |\mathbf{p}^{k+1/4}(\mathbf{x})| + o(a^{-1})$; thus, when a is sufficiently large, $\mathbf{p}^{k+1/4}(\mathbf{x})$ can be approximated by $\mathbf{p}^k(\mathbf{x})$. Meanwhile, since $\tau = O(a^{-2})$, when $p^k \leq (\tau\alpha_0/2)^{1/2}$, we can approximate $\mathbf{p}^{k+1/4}(\mathbf{x})$ by a zero vector.

In a compact form, we deduce the updated formula

$$(3.8) \quad \mathbf{p}^{k+1/4}(\mathbf{x}) = \begin{cases} \mathbf{0} & \text{if } |\mathbf{p}^k(\mathbf{x})|^2 \leq \tau\alpha_0/2, \\ \mathbf{p}^k(\mathbf{x}), & \text{otherwise.} \end{cases}$$

We note that, up to a scaling factor in the threshold, the solution (3.8) is identical to the formula in [62] derived for the discrete L^0 -gradient minimization.

The first equation in (3.3) is the Euler–Lagrange equation of the following minimization problem:

$$\mathbf{p}^{k+2/4} = \arg \min_{\mathbf{q} \in (L^2(\Omega))^2} \left[\frac{1}{2} \int_{\Omega} |\mathbf{q} - \mathbf{p}^{k+1/4}|^2 dx + \tau \alpha_{\text{curv}} \int_{\Omega} |\nabla \cdot \boldsymbol{\lambda}^{k+1/4}|^2 |\mathbf{q}| dx \right],$$

whose closed-form solution is given as

$$(3.9) \quad \mathbf{p}^{k+2/4} = \max \left\{ 0, 1 - \frac{\tau \alpha_{\text{curv}} |\nabla \cdot \boldsymbol{\lambda}^{k+1/4}|^2}{|\mathbf{p}^{k+1/4}|} \right\} \mathbf{p}^{k+1/4}.$$

For the second equation of (3.3), we note that $\boldsymbol{\lambda}^{k+2/4}$ solves

$$(3.10) \quad \boldsymbol{\lambda}^{k+2/4} = \arg \min_{\boldsymbol{\mu} \in (H^1(\Omega))^2} \left[\frac{\gamma_1}{2} \int_{\Omega} |\boldsymbol{\mu} - \boldsymbol{\lambda}^{k+1/4}|^2 d\mathbf{x} + \tau \alpha_{\text{curv}} \int_{\Omega} |\nabla \cdot \boldsymbol{\mu}|^2 |\mathbf{p}^{k+2/4}| d\mathbf{x} \right],$$

and the corresponding Euler–Lagrange equation is

$$(3.11) \quad \begin{cases} \gamma_1 \frac{\boldsymbol{\lambda}^{k+2/4} - \boldsymbol{\lambda}^{k+1/4}}{\tau} - 2\alpha_{\text{curv}} \nabla (|\mathbf{p}^{k+2/4}| \nabla \cdot \boldsymbol{\lambda}^{k+2/4}) = 0 & \text{in } \Omega, \\ |\mathbf{p}^{k+2/4}| \nabla \cdot \boldsymbol{\lambda}^{k+2/4} = 0 & \text{on } \partial\Omega. \end{cases}$$

3.3. On the solution to subproblem (3.4). We update $\mathbf{p}^{k+3/4}$ and $\boldsymbol{\lambda}^{k+3/4}$ using the method proposed in [20, section 3.5]. Note that $\mathbf{p}^{k+3/4}$ and $\boldsymbol{\lambda}^{k+3/4}$ solve

$$(3.12) \quad (\mathbf{p}^{k+3/4}, \boldsymbol{\lambda}^{k+3/4}) = \arg \min_{(\mathbf{q}, \boldsymbol{\mu}) \in S} \left[\frac{1}{2} \int_{\Omega} |\mathbf{q} - \mathbf{p}^{k+2/4}|^2 d\mathbf{x} + \frac{\gamma_1}{2} \int_{\Omega} |\boldsymbol{\mu} - \boldsymbol{\lambda}^{k+2/4}|^2 d\mathbf{x} \right].$$

Problem (3.12) can be solved in a pointwise manner. For each given \mathbf{x} , $(\mathbf{p}^{k+3/4}(\mathbf{x}), \boldsymbol{\lambda}^{k+3/4}(\mathbf{x}))$ satisfies

$$(3.13) \quad (\mathbf{p}^{k+3/4}(\mathbf{x}), \boldsymbol{\lambda}^{k+3/4}(\mathbf{x})) = \arg \min_{(\mathbf{q}(\mathbf{x}), \boldsymbol{\mu}(\mathbf{x})) \in \chi} \left[|\mathbf{q}(\mathbf{x}) - \mathbf{q}^{k+2/4}(\mathbf{x})|^2 + \gamma_1 |\boldsymbol{\mu}(\mathbf{x}) - \boldsymbol{\lambda}^{k+2/4}(\mathbf{x})|^2 \right]$$

with $\chi = \{(\mathbf{a}, \mathbf{b}) \in \mathbb{R}^2 : \mathbf{a} \cdot \mathbf{b} = |\mathbf{a}|, |\mathbf{b}| \leq 1\}$. Define

$$\chi_1 = \{(\mathbf{a}, \mathbf{b}) \in \mathbb{R}^2 : |\mathbf{a}| = 0, |\mathbf{b}| \leq 1\}, \text{ and } \chi_2 = \{(\mathbf{a}, \mathbf{b}) \in \mathbb{R}^2 : |\mathbf{a}| \neq 0, \mathbf{a} \cdot \mathbf{b} = |\mathbf{q}|, |\mathbf{b}| = 1\}.$$

We have that $\chi = \chi_1 \cup \chi_2$. We next discuss the solution of (3.13) on χ_1 and χ_2 separately.

Over χ_1 , denote the solution to (3.13) by $(\hat{\mathbf{p}}^{k+3/4}(\mathbf{x}), \hat{\boldsymbol{\lambda}}^{k+3/4}(\mathbf{x}))$. Problem (3.13) reduces to

$$\hat{\boldsymbol{\lambda}}(\mathbf{x})^{k+3/4} = \arg \min_{\boldsymbol{\mu}(\mathbf{x}) \in \mathbb{R}^2 : |\boldsymbol{\mu}(\mathbf{x})| \leq 1} |\boldsymbol{\mu}(\mathbf{x}) - \boldsymbol{\lambda}^{k+2/4}(\mathbf{x})|^2$$

and $\hat{\mathbf{p}}^{k+3/4}(\mathbf{x}) = \mathbf{0}$. The closed-form solution for $\hat{\boldsymbol{\lambda}}^{k+3/4}(\mathbf{x})$ is given as

$$(3.14) \quad \hat{\boldsymbol{\lambda}}^{k+3/4}(\mathbf{x}) = \frac{\boldsymbol{\lambda}^{k+2/4}(\mathbf{x})}{\max\{1, |\boldsymbol{\lambda}^{k+2/4}(\mathbf{x})|\}}.$$

Over χ_2 , denote the solution to (3.13) by $(\tilde{\mathbf{p}}^{k+3/4}(\mathbf{x}), \tilde{\boldsymbol{\lambda}}^{k+3/4}(\mathbf{x}))$, and it can be written as

$$(3.15) \quad \begin{aligned} & (\tilde{\mathbf{p}}^{k+3/4}(\mathbf{x}), \tilde{\boldsymbol{\lambda}}^{k+3/4}(\mathbf{x})) \\ &= \arg \min_{\substack{(\mathbf{q}(\mathbf{x}), \boldsymbol{\mu}(\mathbf{x})) \in \mathbb{R}^2 \times \mathbb{R}^2, \\ \mathbf{q}(\mathbf{x}) \neq \mathbf{0}, \mathbf{q}(\mathbf{x}) \cdot \boldsymbol{\mu}(\mathbf{x}) = |\mathbf{q}(\mathbf{x})|, \\ |\boldsymbol{\mu}(\mathbf{x})| = 1}} \left[|\mathbf{q}(\mathbf{x}) - \mathbf{p}^{k+2/4}(\mathbf{x})|^2 + \gamma_1 |\boldsymbol{\mu}(\mathbf{x}) - \boldsymbol{\lambda}^{k+2/4}(\mathbf{x})|^2 \right]. \end{aligned}$$

Denote $\theta = |\mathbf{q}(\mathbf{x})|$, $\mathbf{y}(\mathbf{x}) = \mathbf{p}^{k+2/4}(\mathbf{x})$, and $\mathbf{w}(\mathbf{x}) = \boldsymbol{\lambda}^{k+2/4}(\mathbf{x})$ for each $\mathbf{x} \in \Omega$. Problem (3.15) is equivalent to solving

$$(3.16) \quad \min_{(\theta, \boldsymbol{\mu}(\mathbf{x})) \in \mathbb{R} \times \mathbb{R}^2, \theta > 0, |\boldsymbol{\mu}(\mathbf{x})|=1} [\theta^2 - 2\theta \boldsymbol{\mu}(\mathbf{x}) \cdot \mathbf{y}(\mathbf{x}) - 2\gamma_1 \boldsymbol{\mu}(\mathbf{x}) \cdot \mathbf{w}(\mathbf{x})].$$

For a fixed θ , the solution $\boldsymbol{\mu}^*(\mathbf{x}, \theta)$ of (3.16) is given by

$$(3.17) \quad \boldsymbol{\mu}^*(\mathbf{x}, \theta) = \frac{\theta \mathbf{y}(\mathbf{x}) + \gamma_1 \mathbf{w}(\mathbf{x})}{|\theta \mathbf{y}(\mathbf{x}) + \gamma_1 \mathbf{w}(\mathbf{x})|}.$$

Substituting (3.17) to (3.16) leads to

$$(3.18) \quad \min_{\theta > 0} [\theta^2 - 2|\theta \mathbf{y}(\mathbf{x}) + \gamma_1 \mathbf{w}(\mathbf{x})|].$$

We solve (3.18) by a fixed-point method. Denote

$$E(\mathbf{x}, \theta) = \theta^2 - 2|\theta \mathbf{y}(\mathbf{x}) + \gamma_1 \mathbf{w}(\mathbf{x})|,$$

and thus,

$$(3.19) \quad \frac{dE}{d\theta}(\mathbf{x}, \theta) = 2\theta - \frac{2\mathbf{y}(\mathbf{x}) \cdot (\theta \mathbf{y}(\mathbf{x}) + \gamma_1 \mathbf{w}(\mathbf{x}))}{|\theta \mathbf{y}(\mathbf{x}) + \gamma_1 \mathbf{w}(\mathbf{x})|}.$$

We initialize $\theta^0 = |\mathbf{y}(\mathbf{x})|$. For $m = 0, 1, 2, \dots$, we update θ^{m+1} from θ^m via

$$(3.20) \quad \theta^{m+1} = \max \left\{ 0, \frac{\mathbf{y}(\mathbf{x}) \cdot (\theta^m \mathbf{y}(\mathbf{x}) + \gamma_1 \mathbf{w}(\mathbf{x}))}{|\theta^m \mathbf{y}(\mathbf{x}) + \gamma_1 \mathbf{w}(\mathbf{x})|} \right\}$$

until $|\theta^{m+1} - \theta^m| < \varepsilon$ for some small $\varepsilon > 0$.

Denote the converged θ by $\theta^*(\mathbf{x})$; then, we compute

$$(3.21) \quad \tilde{\boldsymbol{\lambda}}^{k+3/4}(\mathbf{x}) = \frac{\theta^*(\mathbf{x}) \mathbf{p}^{k+2/4}(\mathbf{x}) + \gamma_1 \boldsymbol{\lambda}^{k+2/4}(\mathbf{x})}{|\theta^*(\mathbf{x}) \mathbf{p}^{k+2/4}(\mathbf{x}) + \gamma_1 \boldsymbol{\lambda}^{k+2/4}(\mathbf{x})|}, \quad \tilde{\mathbf{p}}^{k+3/4}(\mathbf{x}) = \theta^* \tilde{\boldsymbol{\lambda}}^{k+3/4}(\mathbf{x}).$$

Finally, we define

$$G(\mathbf{q}, \boldsymbol{\mu}; \mathbf{x}) = |\mathbf{q}(\mathbf{x}) - \mathbf{q}^{k+2/4}(\mathbf{x})|^2 + \gamma_1 |\boldsymbol{\mu}(\mathbf{x}) - \boldsymbol{\lambda}^{k+2/4}(\mathbf{x})|^2$$

and compare the minimizers in χ_1 and χ_2 to obtain $(\mathbf{p}^{k+3/4}(\mathbf{x}), \boldsymbol{\lambda}^{k+3/4}(\mathbf{x}))$ because

$$(3.22) \quad (\mathbf{p}^{k+3/4}(\mathbf{x}), \boldsymbol{\lambda}^{k+3/4}(\mathbf{x})) = \begin{cases} (\hat{\mathbf{p}}^{k+3/4}(\mathbf{x}), \hat{\boldsymbol{\lambda}}^{k+3/4}(\mathbf{x})) & \text{if } G(\hat{\mathbf{p}}^{k+3/4}, \hat{\boldsymbol{\lambda}}^{k+3/4}; \mathbf{x}) \\ & \leq G(\tilde{\mathbf{p}}^{k+3/4}, \tilde{\boldsymbol{\lambda}}^{k+3/4}; \mathbf{x}), \\ (\tilde{\mathbf{p}}^{k+3/4}(\mathbf{x}), \tilde{\boldsymbol{\lambda}}^{k+3/4}(\mathbf{x})), & \text{otherwise.} \end{cases}$$

Remark 3.2. The operator in (3.19) is nonlinear, nonsmooth, and may be discontinuous (depending on the angle between $\mathbf{y}(\mathbf{x})$ and $\mathbf{w}(\mathbf{x})$). Proving the convergence of the fixed-point iteration (3.20) requires a careful analysis of the properties of \mathbf{y} and \mathbf{w} and an independent study. Intuitively, with a small time step τ , after each iteration, we expect that $(\mathbf{p}^{k+2/4}, \boldsymbol{\lambda}^{k+2/4})$ stays close to $(\mathbf{p}^{(k-1)+3/4}, \boldsymbol{\lambda}^{(k-1)+3/4})$ and does not deviate too far from the set S . Iteration (3.20) is expected to converge. Numerically, (3.20) converges in our experiments.

3.4. On the solution to subproblem (3.5). In (3.5), $(\mathbf{p}^{k+1}, r^{k+1}, \mathbf{s}^{k+1})$ solves

$$(3.23) \quad \min_{\substack{(\mathbf{q}, w, \mathbf{g}) \in \Sigma_f, w \in H^2(\Omega), \\ \mathbf{g} \in (H^1(\Omega))^2}} \left[\frac{1}{2} \int_{\Omega} |\mathbf{q} - \mathbf{p}^{k+3/4}|^2 d\mathbf{x} + \frac{\gamma_2}{2} \int_{\Omega} |w - r^{k+3/4}|^2 d\mathbf{x} + \frac{\gamma_3}{2} \int_{\Omega} |\mathbf{g} - \mathbf{s}^{k+3/4}|^2 d\mathbf{x} \right. \\ \left. + \tau \alpha_w \int_{\Omega} |\Delta w|^2 d\mathbf{x} + \tau \alpha_n \int_{\Omega} |\mathbf{g}|^2 d\mathbf{x} + \frac{\tau}{2} \int_{\Omega} |f - (v_{\mathbf{q}, w, \mathbf{g}} + w + \nabla \cdot \mathbf{g})|^2 d\mathbf{x} \right],$$

or equivalently,

$$(3.24) \quad \begin{cases} (v^{k+1}, r^{k+1}, \mathbf{s}^{k+1}) = \arg \min_{\substack{v \in H^1(\Omega), w \in H^2(\Omega), \\ \mathbf{g} \in (H^1(\Omega))^2}} \left[\frac{1}{2} \int_{\Omega} |\nabla v - \mathbf{p}^{k+3/4}|^2 d\mathbf{x} + \frac{\gamma_2}{2} \int_{\Omega} |w - r^{k+3/4}|^2 d\mathbf{x} \right. \\ \left. + \frac{\gamma_3}{2} \int_{\Omega} |\mathbf{g} - \mathbf{s}^{k+3/4}|^2 d\mathbf{x} + \tau \alpha_w \int_{\Omega} |\Delta w|^2 d\mathbf{x} + \tau \alpha_n \int_{\Omega} |\mathbf{g}|^2 d\mathbf{x} \right. \\ \left. + \frac{\tau}{2} \int_{\Omega} |f - (v + w + \nabla \cdot \mathbf{g})|^2 d\mathbf{x} \right], \\ \mathbf{p}^{k+1} = \nabla v^{k+1}. \end{cases}$$

The optimality condition for $(v^{k+1}, r^{k+1}, \mathbf{s}^{k+1})$ is

$$(3.25) \quad \begin{cases} \begin{cases} \frac{-\Delta v^{k+1} + \nabla \cdot \mathbf{p}^{k+3/4}}{\tau} + v^{k+1} - (f - r^{k+1} - \nabla \cdot \mathbf{s}^{k+1}) = 0 & \text{in } \Omega, \\ (\nabla v^{k+1} - \mathbf{p}^{k+3/4}) \cdot \mathbf{n} = 0 & \text{on } \partial\Omega, \end{cases} \\ \begin{cases} \gamma_2 \frac{r^{k+1} - r^{k+3/4}}{\tau} + r^{k+1} - (f - v^{k+1} - \nabla \cdot \mathbf{s}^{k+1}) + 2\alpha_w (\nabla^4 r^{k+1}) = 0 & \text{in } \Omega, \\ \Delta r^{k+1} = 0, \nabla^3 r^{k+1} \cdot \mathbf{n} = 0 & \text{on } \partial\Omega, \end{cases} \\ \begin{cases} \gamma_3 \frac{\mathbf{s}^{k+1} - \mathbf{s}^{k+3/4}}{\tau} - \nabla (\nabla \cdot \mathbf{s}^{k+1}) + 2\alpha_n \mathbf{s}^{k+1} + \nabla (f - v^{k+1} - r^{k+1}) = 0 & \text{in } \Omega, \\ f - (v^{k+1} + r^{k+1} + \nabla \cdot \mathbf{s}^{k+1}) = 0 & \text{on } \partial\Omega. \end{cases} \end{cases}$$

The proposed operator-splitting scheme is summarized in Algorithm 3.1.

3.5. Adapt to periodic boundary conditions for efficiency. We note that, while (3.11) and (3.25) contain high-order derivatives, they are linear. Therefore, we can leverage the FFT to convert these PDE systems to pointwise algebraic systems, for which we can deduce explicit solutions. To garnish such computational efficiency, we extend our model (2.1) to periodic data, and this requires equipping several equations with the periodic boundary condition. Specifically, in (2.12), (2.10), (3.10), (3.11), (3.23), (3.24), and (3.25), we equip functions spaces with the periodic boundary condition or replace the boundary conditions by the periodic one. We defer the details to Appendix C.

In the rest of this paper, we always assume these adaptations and consider the periodic boundary condition.

4. Numerical discretization. In this section, we provide implementation details for solving the proposed minimization problem.

Algorithm 3.1 Proposed operator-splitting algorithm.

Require: Gray image f ; model parameters: $\alpha_0, \alpha_{\text{curv}}, \alpha_w, \alpha_n$; algorithmic parameters: time step τ , evolution speed factor $\gamma_i, i = 1, 2, 3$, threshold ρ for termination, maximal number of iteration Iter_{\max} .

- 1: **for** $k = 1, \dots, \text{Iter}_{\max}$ **do**
- 2: Update $\mathbf{p}^k \rightarrow \mathbf{p}^{k+1/4}$ by (3.8), and set $\boldsymbol{\lambda}^{k+1/4} = \boldsymbol{\lambda}^k, r^{k+1/4} = r^k, \mathbf{s}^{k+1/4} = \mathbf{s}^k$.
- 3: Update $\mathbf{p}^{n+1/4} \rightarrow \mathbf{p}^{k+2/4}$ by (3.9) and $\boldsymbol{\lambda}^{k+1/4} \rightarrow \boldsymbol{\lambda}^{k+2/4}$ by solving (3.11), and set $r^{k+2/4} = r^{k+1/4}, \mathbf{s}^{k+2/4} = \mathbf{s}^{k+1/4}$.
- 4: Update $\mathbf{p}^{k+2/4} \rightarrow \mathbf{p}^{k+3/4}$ and $\boldsymbol{\lambda}^{k+2/4} \rightarrow \boldsymbol{\lambda}^{k+3/4}$ by (3.22), and set $r^{k+3/4} = r^{k+2/4}, \mathbf{s}^{k+3/4} = \mathbf{s}^{k+2/4}$.
- 5: Compute v^{k+1}, r^{k+1} , and \mathbf{s}^{k+1} by solving (3.25), and set $\mathbf{p}^{k+1} = \nabla v^{k+1}, n^{k+1} = \nabla \cdot \mathbf{s}^{k+1}, \boldsymbol{\lambda}^{k+1} = \boldsymbol{\lambda}^{k+3/4}$.
- 6: **if** $\max\left\{\frac{\|r^{k+1}-r^k\|_2}{\|r^k\|_2}, \frac{\|v^{k+1}-v^n\|_2}{\|v^n\|_2}\right\} < \rho$ **then**
- 7: break.
- 8: **end if**
- 9: **end for**
- 10: **return** the converged homogeneous structure v^* , smooth part w^* , and oscillatory part n^* such that f is approximated by $v^* + w^* + n^*$.

4.1. Synopsis. Let Ω be a rectangular domain with $M \times N$ pixels. Denote the two spatial directions by x_1, x_2 with step size $\Delta x_1 = \Delta x_2 = h$ for some $h > 0$. For an image f defined on Ω , we denote $f(i, j) = f(ih, jh)$. Assume that f satisfies the periodic boundary condition. We define the backward (−) and forward (+) approximation for $\partial f / \partial x_1$ and $\partial f / \partial x_2$ as

$$\begin{aligned} \partial_1^- f(i, j) &= \begin{cases} \frac{f(i, j) - f(i-1, j)}{h} & 1 < i \leq M, \\ \frac{f(1, j) - f(M, j)}{h} & i = 1, \end{cases} & \partial_1^+ f(i, j) &= \begin{cases} \frac{f(i+1, j) - f(i, j)}{h} & 1 \leq i < M, \\ \frac{f(1, j) - f(M, j)}{h} & i = M, \end{cases} \\ \partial_2^- f(i, j) &= \begin{cases} \frac{f(i, j) - f(i, j-1)}{h} & 1 < i \leq N, \\ \frac{f(i, 1) - f(i, N)}{h} & i = 1, \end{cases} & \partial_2^+ f(i, j) &= \begin{cases} \frac{f(i, j+1) - f(i, j)}{h} & 1 \leq i < N, \\ \frac{f(i, 1) - f(i, N)}{h} & i = N. \end{cases} \end{aligned}$$

For any scalar-valued function f and vector-valued function $\mathbf{p} = (p_1, p_2)$, the backward (−) and forward (+) approximation for gradient and divergence are defined as

$$\nabla^\pm f(i, j) = (\partial_1^\pm f(i, j), \partial_2^\pm f(i, j)), \quad \text{div}^\pm \mathbf{p}(i, j) = \partial_1^\pm p_1(i, j) + \partial_2^\pm p_2(i, j).$$

The discretized Laplacian is defined as

$$\Delta f(i, j) = \text{div}^-(\nabla^+ f(i, j)) = \partial_1^- \partial_1^+ f(i, j) + \partial_2^- \partial_2^+ f(i, j),$$

which recovers the central difference scheme.

Define the shifting and identity operator as

$$(\mathcal{S}_1^\pm f)(i, j) = f(i \pm 1, j), \quad (\mathcal{S}_2^\pm f)(i, j) = f(i, j \pm 1), \quad (\mathcal{I}f)(i, j) = f(i, j),$$

where the periodic boundary condition is assumed. Denote the discrete Fourier transform and its inverse by \mathcal{F} and \mathcal{F}^{-1} , respectively. We have that

$$\mathcal{F}(\mathcal{S}_1^\pm f)(i, j) = e^{\pm 2\pi\sqrt{-1}(i-1)/M} \mathcal{F}(f)(i, j), \text{ and } \mathcal{F}(\mathcal{S}_2^\pm f)(i, j) = e^{\pm 2\pi\sqrt{-1}(j-1)/N} \mathcal{F}(f)(i, j).$$

We use $\text{Real}(\cdot)$ to denote the real part of a complex quantity.

4.2. Discrete analogue of $\mathbf{p}^{k+1/4}$, $\mathbf{p}^{k+2/4}$ and $\boldsymbol{\lambda}^{k+2/4}$. For $\mathbf{p}^{k+1/4}$, we discretize (3.8) as

$$(4.1) \quad \mathbf{p}^{k+1/4}(i, j) = \begin{cases} \mathbf{0} & \text{if } (p_1^k(i, j))^2 + (p_2^k(i, j))^2 \leq \alpha_0 \tau / 2, \\ \mathbf{p}^k(i, j), & \text{otherwise,} \end{cases}$$

and the computational cost is $\mathcal{O}(MN)$.

According to (3.9), $\mathbf{p}^{k+2/4}$ is updated pointwisely. We thus have that

$$(4.2) \quad \mathbf{p}^{k+2/4}(i, j) = \max \left\{ 0, 1 - \frac{\tau \alpha_w |\text{div}^- \boldsymbol{\lambda}^{k+1/4}(i, j)|^2}{\sqrt{(p_1^{k+1/4}(i, j))^2 + (p_2^{k+2/4}(i, j))^2}} \right\} \mathbf{p}^{k+1/4}(i, j),$$

whose computational cost is $\mathcal{O}(MN)$.

To compute $\boldsymbol{\lambda}^{k+2/4} = (\lambda_1^{k+2/4}, \lambda_2^{k+2/4})$, the updating formula (3.11) can be rewritten as

$$(4.3) \quad \gamma_1 \boldsymbol{\lambda}^{k+2/4} - 2\tau \alpha_w \nabla(|\mathbf{p}^{k+2/4}| \nabla \cdot \boldsymbol{\lambda}^{k+2/4}) = \gamma_1 \boldsymbol{\lambda}^{k+1/4}.$$

Instead of directly solving (4.3), we use the frozen coefficient method [55, 32, 41] and consider the approximation

$$(4.4) \quad \gamma_1 \boldsymbol{\lambda}^{k+2/4} - c \nabla(\nabla \cdot \boldsymbol{\lambda}^{k+2/4}) = \gamma_1 \boldsymbol{\lambda}^{k+1/4} - c \nabla(\nabla \cdot \boldsymbol{\lambda}^{k+1/4}) + 2\tau \alpha_w \nabla(|\mathbf{p}^{k+2/4}| \nabla \cdot \boldsymbol{\lambda}^{k+1/4})$$

for some small coefficient $c > 0$. In our experiment, we set $c = 1 \times 10^{-9}$. We discretize (4.4) as

$$(4.5) \quad \begin{aligned} & \gamma_1 \boldsymbol{\lambda}^{k+2/4} - c \nabla^+(\text{div}^- \boldsymbol{\lambda}^{k+2/4}) \\ &= \gamma_1 \boldsymbol{\lambda}^{k+1/4} - c \nabla^+(\text{div}^- \boldsymbol{\lambda}^{k+1/4}) + 2\tau \alpha_w \nabla^+(|\mathbf{p}^{k+2/4}|(\text{div}^- \boldsymbol{\lambda}^{k+1/4})). \end{aligned}$$

Equation (4.5) can be written in a matrix form as

$$(4.6) \quad \begin{pmatrix} \gamma_1 - c \partial_1^+ \partial_1^- & -c \partial_1^+ \partial_2^- \\ -c \partial_2^+ \partial_1^- & \gamma_1 - c \partial_2^+ \partial_2^- \end{pmatrix} \begin{pmatrix} \lambda_1^{k+2/4} \\ \lambda_2^{k+2/4} \end{pmatrix} = \begin{pmatrix} b_1 \\ b_2 \end{pmatrix}$$

with

$$\begin{cases} b_1 = \gamma_1 \lambda_1^{k+1/4} - c \partial_1^+(\text{div}^- \boldsymbol{\lambda}^{k+1/4}) + 2\tau \alpha_w \partial_1^+(|\mathbf{p}^{k+2/4}|(\text{div}^- \boldsymbol{\lambda}^{k+1/4})), \\ b_2 = \gamma_1 \lambda_2^{k+1/4} - c \partial_2^+(\text{div}^- \boldsymbol{\lambda}^{k+1/4}) + 2\tau \alpha_w \partial_2^+(|\mathbf{p}^{k+2/4}|(\text{div}^- \boldsymbol{\lambda}^{k+1/4})). \end{cases}$$

System (4.6) is equivalent to

$$(4.7) \quad \begin{pmatrix} \gamma_1 - c(\mathcal{S}_1^+ - \mathcal{I})(\mathcal{I} - \mathcal{S}_1^-)/h^2 & -c(\mathcal{S}_1^+ - \mathcal{I})(\mathcal{I} - \mathcal{S}_2^-)/h^2 \\ -c(\mathcal{S}_2^+ - \mathcal{I})(\mathcal{I} - \mathcal{S}_1^-)/h^2 & \gamma_1 - c(\mathcal{S}_2^+ - \mathcal{I})(\mathcal{I} - \mathcal{S}_2^-)/h^2 \end{pmatrix} \begin{pmatrix} \lambda_1^{k+2/4} \\ \lambda_2^{k+2/4} \end{pmatrix} = \begin{pmatrix} b_1 \\ b_2 \end{pmatrix}.$$

Applying discrete Fourier transform on both sides of (4.7) gives

$$(4.8) \quad \begin{pmatrix} a_{11} & a_{12} \\ a_{21} & a_{22} \end{pmatrix} \mathcal{F} \begin{pmatrix} \mu_1^{k+2/4} \\ \mu_2^{k+2/4} \end{pmatrix} = \mathcal{F} \begin{pmatrix} b_1 \\ b_2 \end{pmatrix},$$

where

$$\begin{aligned} a_{11}(i, j) &= \gamma_1 - 2c(\cos \zeta_i - 1)/h^2, \quad a_{22}(i, j) = \gamma_1 - 2c(\cos \eta_j - 1)/h^2, \\ a_{12}(i, j) &= c(\cos \zeta_i + \sqrt{-1} \sin \zeta_i - 1)(\cos \eta_j - \sqrt{-1} \sin \eta_j - 1)/h^2, \\ a_{21}(i, j) &= c(\cos \eta_j + \sqrt{-1} \sin \eta_j - 1)(\cos \zeta_i - \sqrt{-1} \sin \zeta_i - 1)/h^2 \end{aligned}$$

with $\zeta_i = 2\pi(i-1)/M$, $\eta_j = 2\pi(j-1)/N$ for $i = 1, \dots, M$ and $j = 1, \dots, N$. We thus update $\lambda^{k+2/4}$ via

$$(4.9) \quad \begin{pmatrix} \lambda_1^{k+2/4} \\ \lambda_2^{k+2/4} \end{pmatrix} = \text{Real} \left(\mathcal{F}^{-1} \left[\frac{1}{a_{11}a_{22} - a_{12}a_{21}} \begin{pmatrix} a_{11}\mathcal{F}(b_1) - a_{12}\mathcal{F}(b_2) \\ -a_{21}\mathcal{F}(b_1) + a_{22}\mathcal{F}(b_2) \end{pmatrix} \right] \right).$$

Since the linear system is solved explicitly under the forward and inverse FFT, the computational cost is $\mathcal{O}(MN(\log M + \log N))$.

4.3. Discrete analogue of $\mathbf{p}^{k+3/4}$, $\boldsymbol{\lambda}^{k+3/4}$. According to section 3.3, $\mathbf{p}^{k+3/4}$ and $\boldsymbol{\lambda}^{k+3/4}$ can be computed pointwisely. On χ_1 , for each i, j , we set $\hat{\mathbf{p}}^{k+3/4}(i, j) = \mathbf{0}$ and discretize (3.14) as

$$(4.10) \quad \hat{\boldsymbol{\lambda}}^{k+3/4}(i, j) = \frac{\boldsymbol{\lambda}^{k+2/4}(i, j)}{\max \left\{ 1, \sqrt{|\boldsymbol{\lambda}^{k+2/4}(i, j)|^2} \right\}}.$$

On χ_2 , we discretize (3.21) as

$$\hat{\boldsymbol{\lambda}}^{k+3/4}(i, j) = \frac{\theta^* \mathbf{p}^{k+2/4}(i, j) + \gamma_1 \boldsymbol{\lambda}^{k+2/4}(i, j)}{|\theta^* \mathbf{p}^{k+2/4}(i, j) + \gamma_1 \boldsymbol{\lambda}^{k+2/4}(i, j)|}, \quad \tilde{\mathbf{p}}^{k+3/4}(i, j) = \theta^* \hat{\boldsymbol{\lambda}}^{k+3/4}(i, j),$$

where θ^* is computed by (3.20) with $\mathbf{y}(\mathbf{x}) = \mathbf{p}^{k+2/4}(i, j)$, $\mathbf{w}(\mathbf{x}) = \boldsymbol{\lambda}^{k+2/4}(i, j)$. Functions $\mathbf{p}^{k+3/4}$ and $\boldsymbol{\lambda}^{k+3/4}$ are then updated using (3.22).

4.4. Discrete analogue of \mathbf{p}^{k+1} , \mathbf{r}^{k+1} and \mathbf{s}^{k+1} . Reorganizing the system (3.25), we get a linear system in v^{k+1}, r^{k+1} , and $\mathbf{s}^{k+1} = (s_1^{k+1}, s_2^{k+1})$:

$$(4.11) \quad \begin{cases} (-\Delta + \tau I)v^{k+1} + \tau r^{k+1} + \tau \nabla \cdot \mathbf{s}^{k+1} = -\nabla \cdot \mathbf{p}^{k+3/4} + \tau f, \\ \tau v^{k+1} + [(\gamma_2 + \tau)I + 2\tau \alpha_w \nabla^4]r^{k+1} + \tau \nabla \cdot \mathbf{s}^{k+1} = \gamma_2 r^{k+3/4} + \tau f, \\ -\tau \nabla v^{k+1} - \tau \nabla r^{k+1} + [(\gamma_3 + 2\tau \alpha_n)I - \tau \nabla \operatorname{div}] \mathbf{s}^{k+1} = \gamma_3 \mathbf{s}^{k+3/4} - \tau \nabla f. \end{cases}$$

Upon discretization, we obtain a linear system

$$\mathbf{A} \begin{bmatrix} v^{k+1} \\ r^{k+1} \\ s_1^{k+1} \\ s_2^{k+1} \end{bmatrix} = \begin{bmatrix} b_1^k \\ b_2^k \\ b_3^k \\ b_4^k \end{bmatrix} \quad \text{with} \quad \begin{cases} b_1^k = -\operatorname{div}^- \mathbf{p}^{k+3/4} + \tau f, \\ b_2^k = \gamma_2 r^{k+3/4} + \tau f, \\ b_3^k = \gamma_3 s_1^{k+3/4} - \tau \partial_1^+ f, \\ b_4^k = \gamma_3 s_2^{k+3/4} - \tau \partial_2^+ f, \end{cases}$$

where

$$\mathbf{A} = \begin{bmatrix} -\frac{1}{h^2} & & & \\ -\frac{1}{h^2} \cdot & & & \\ [(\mathcal{I} - \mathcal{S}_1^-)(\mathcal{S}_1^+ - \mathcal{I}) & \tau & \tau(\mathcal{I} - \mathcal{S}_1^-)/h & \tau(\mathcal{I} - \mathcal{S}_2^-)/h \\ + (\mathcal{I} - \mathcal{S}_2^-)(\mathcal{S}_2^+ - \mathcal{I})] & & & \\ + \tau \mathcal{I} & & & \\ \tau & (\gamma_2 + \tau)\mathcal{I} & \tau(\mathcal{I} - \mathcal{S}_1^-)/h & \tau(\mathcal{I} - \mathcal{S}_2^-)/h \\ & + 2\tau\alpha_w \mathcal{P} & & \\ -\tau(\mathcal{S}_1^+ - \mathcal{I})/h & -\tau(\mathcal{S}_1^+ - \mathcal{I})/h & \frac{\gamma_3 + 2\tau\alpha_n -}{h^2} (\mathcal{S}_1^+ - \mathcal{I})(\mathcal{I} - \mathcal{S}_1^-) & -\frac{\tau}{h^2} (\mathcal{S}_1^+ - \mathcal{I})(\mathcal{I} - \mathcal{S}_2^-) \\ -\tau(\mathcal{S}_2^+ - \mathcal{I})/h & -\tau(\mathcal{S}_2^+ - \mathcal{I})/h & -\frac{\tau}{h^2} (\mathcal{S}_2^+ - \mathcal{I})(\mathcal{I} - \mathcal{S}_1^-) & \frac{\gamma_3 + 2\tau\alpha_n -}{h^2} (\mathcal{S}_2^+ - \mathcal{I})(\mathcal{I} - \mathcal{S}_2^-) \end{bmatrix}$$

with

$$\mathcal{P} = \frac{1}{h^4} [((\mathcal{I} - \mathcal{S}_1^-)(\mathcal{S}_1^+ - \mathcal{I}))^2 + (\mathcal{I} - \mathcal{S}_2^-)(\mathcal{S}_2^+ - \mathcal{I})(\mathcal{I} - \mathcal{S}_1^-)(\mathcal{S}_1^+ - \mathcal{I}) \\ + (\mathcal{I} - \mathcal{S}_1^-)(\mathcal{S}_1^+ - \mathcal{I})(\mathcal{I} - \mathcal{S}_2^-)(\mathcal{S}_2^+ - \mathcal{I}) + ((\mathcal{I} - \mathcal{S}_2^-)(\mathcal{S}_2^+ - \mathcal{I}))^2].$$

Note that \mathcal{A} does not depend on the iteration; thus, it can be constructed beforehand and applied repeatedly in each iteration. Applying the discrete Fourier transform \mathcal{F} , we get

$$(4.12) \quad \mathbf{D} \mathcal{F} \begin{pmatrix} \begin{bmatrix} v^{k+1} \\ r^{k+1} \\ s_1^{k+1} \\ s_2^{k+1} \end{bmatrix} \end{pmatrix} = \mathcal{F} \begin{pmatrix} \begin{bmatrix} b_1^k \\ b_2^k \\ b_3^k \\ b_4^k \end{bmatrix} \end{pmatrix}$$

with $\mathbf{D} \in \mathbb{R}^{4 \times 4}$, whose (l, m) th entries d_{lm} , $1 \leq l, m \leq 4$ are listed below.

$$\begin{aligned} d_{11}(i, j) &= (\tau - 2(\cos \zeta_i - 1)/h^2 - 2(\cos \eta_j - 1)/h^2), \quad d_{12} = \tau, \\ d_{13}(i, j) &= \tau[1 - (\cos \zeta_i - \sqrt{-1} \sin \zeta_i)]/h, \quad d_{14}(i, j) = \tau[1 - (\cos \eta_j - \sqrt{-1} \sin \eta_j)]/h, \\ d_{21} &= \tau, \\ d_{22}(i, j) &= \gamma_2 + \tau + 2\tau\alpha_w \frac{4}{h^4} [(\cos \zeta_i - 1)^2 + 2(\cos \zeta_i - 1)(\cos \eta_j - 1) + (\cos \eta_j - 1)^2], \\ d_{23} &= d_{13}, \quad d_{24} = d_{14}, \\ d_{31}(i, j) &= d_{32}(i, j) = -\tau(\cos \zeta_i + \sqrt{-1} \sin \zeta_i - 1)/h, \\ d_{33}(i, j) &= \gamma_3 + 2\tau\alpha_n - 2\tau(\cos \zeta_i - 1)/h^2, \\ d_{34}(i, j) &= \tau(\cos \zeta_i + \sqrt{-1} \sin \zeta_i - 1)(\cos \eta_j - \sqrt{-1} \sin \eta_j - 1)/h^2, \\ d_{41}(i, j) &= d_{42}(i, j) = -\tau(\cos \eta_j + \sqrt{-1} \sin \eta_j - 1)/h, \\ d_{43}(i, j) &= \tau(\cos \eta_j + \sqrt{-1} \sin \eta_j - 1)(\cos \zeta_i - \sqrt{-1} \sin \zeta_i - 1)/h^2, \\ d_{44}(i, j) &= \gamma_3 + 2\tau\alpha_n - 2\tau(\cos \eta_j - 1)/h^2. \end{aligned}$$

To stabilize the computation, we add a small constant $\kappa = 1 \times 10^{-9}$ on the diagonal of \mathbf{D} . The inverse \mathbf{D}^{-1} can be explicitly computed using Cramer's rule. We can efficiently get v^{k+1}, r^{k+1} , and \mathbf{s}^{k+1} by inverse FFT

$$(4.13) \quad \begin{bmatrix} v^{k+1} \\ r^{k+1} \\ s_1^{k+1} \\ s_2^{k+1} \end{bmatrix} = \text{Real} \left(\mathcal{F}^{-1} \left[\mathbf{D}^{-1} \mathcal{F} \left(\begin{bmatrix} b_1^k \\ b_2^k \\ b_3^k \\ b_4^k \end{bmatrix} \right) \right] \right).$$

Similarly to (4.9), as we obtain the updated variables by explicit formula, the computational cost is still $\mathcal{O}(MN(\log M + \log N))$. Overall, the computational cost of a single iteration of our proposed algorithm that updates $(\mathbf{p}^k, \boldsymbol{\lambda}^k, r^k, \mathbf{s}^k)$ to $(\mathbf{p}^{k+1}, \boldsymbol{\lambda}^{k+1}, r^{k+1}, \mathbf{s}^{k+1})$ is on the order of $\mathcal{O}(MN(\log M + \log N))$.

5. Numerical experiments. In this section, we present various experiments to show the behaviors of the proposed model, analyze the effects of model parameters, and justify its effectiveness in the task of decomposition and denoising by ablation and comparison studies. To evaluate the image quality, we employ the Peak Signal-to-Noise Ratio (PSNR) metric

$$\text{PSNR}(u_{\text{ref}}, \hat{u}) = 10 \log_{10} \left(\frac{1}{\|\hat{u} - u_{\text{ref}}\|_2} \right),$$

where u_{ref} is the reference image, \hat{u} is the corresponding approximation, and their intensity values are scaled to $[0, 1]$. We test our method on various synthetic images as well as grayscale photos. For model parameters $\alpha_0, \alpha_{\text{curv}}, \alpha_w$, and α_n , we discuss their selections in section 5.5 and fine-tune them according to the image contents. For algorithmic parameters, we fix $\tau = 0.1, \gamma_1 = 1.0, \gamma_2 = 0.01$, and $\gamma_3 = 20$. We set the global constants for numerical stability $c = 1 \times 10^{-9}$ and $\kappa = 1 \times 10^{-9}$; here, c is the frozen coefficient in (4.4), and κ is added to the diagonal of \mathbf{D} in (4.12) for stability. We take the maximal number of iterations $\text{Iter}_{\max} = 1000$, and fix the threshold for the terminating condition $\rho = 1 \times 10^{-6}$; i.e., the algorithm is terminated if $\max\left\{\frac{\|r^{k+1} - r^k\|_2}{\|r^k\|_2}, \frac{\|v^{k+1} - v^k\|_2}{\|v^k\|_2}\right\} < \rho$. For the default initial conditions, we fix $v_0 = 0.001 \times \tilde{f} + 0.999 \times 0.5$, where \tilde{f} is the input f convolved with a standard Gaussian kernel, $\mathbf{p}_0 = \nabla^+ v_0$, $r_0 = f - v_0$, and $\boldsymbol{\lambda}_0 = \mathbf{s}_0 = \mathbf{0}$. To reduce the boundary artifacts, we pad the input with 30 pixels on each side in a symmetric manner. The algorithm is implemented with MATLAB 2022a in the environment of Windows 11, and all the experiments are conducted in a laptop equipped with 12th Gen Intel(R) Core(TM) i7-12800H, 2400 Mhz, and 14 cores.

5.1. General performances. We illustrate general performances of the proposed model using two sets of experiments. In Figure 3, we show the decomposition results for synthetic images generated by convex combinations of piecewise constant components and smoothly varying shades. In Figure 5, we show the results for grayscale photos with richer details. For both sets of examples, Gaussian noise with intensity $\sigma = 20/255$ is added.

In the first row of Figure 3, a white cross on a black background has a soft round light superimposed over the center. The proposed model successfully extracts the cross v^* where the intensity variation due to the lighting is removed, and the important geometric features such as sharp corners as well as straight boundaries are accurately reconstructed. The lighting

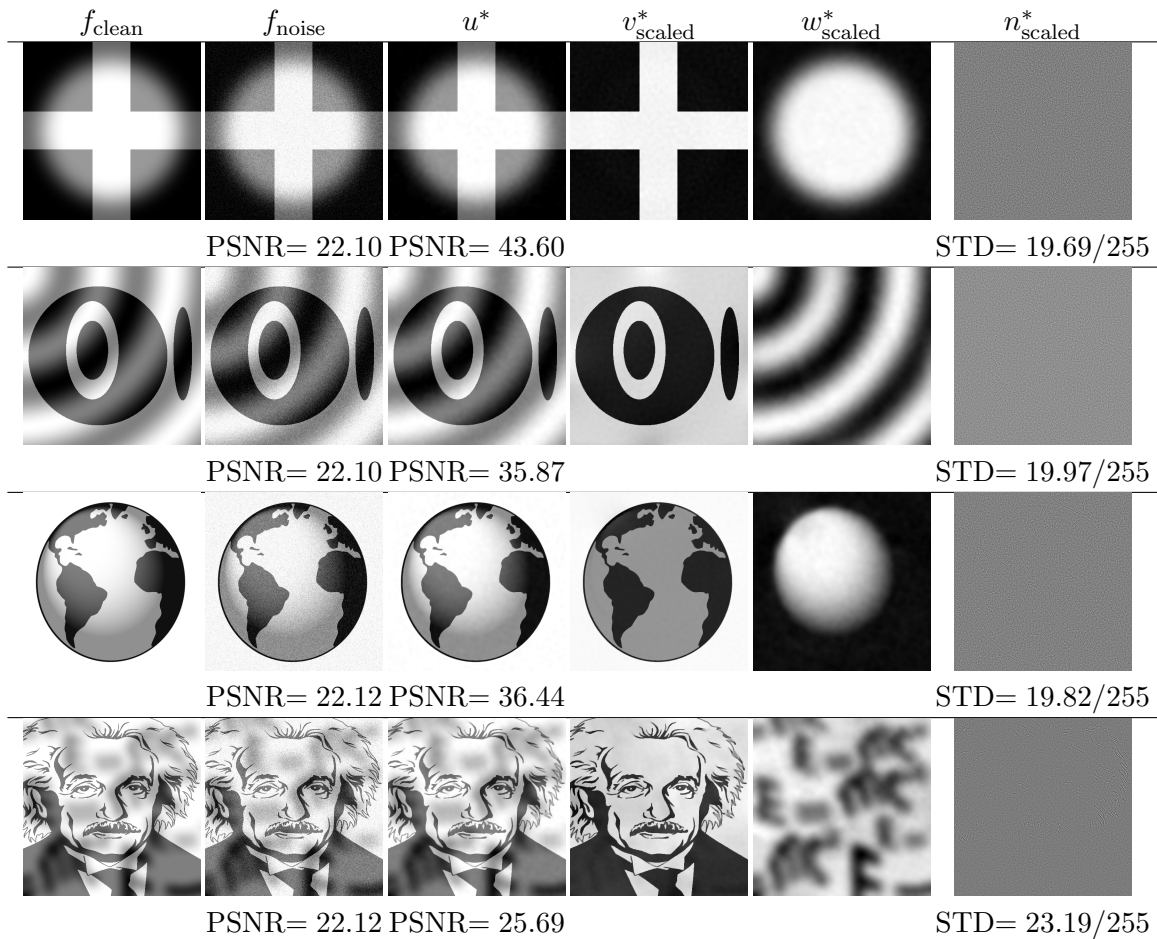


Figure 3. Decomposition of synthetic images with noise ($\sigma = 20/255$). The first column (f_{clean}) shows the clean images; the second column (f_{noise}) shows the noisy inputs; the third column (u^*) shows summations of the identified v^* and w^* components; the subsequent columns show, respectively, v^* , w^* , and n^* , and for visualization, they are linearly scaled between 0 and 1. Model parameters for these examples are $\alpha_0 = 2 \times 10^{-2}$, $\alpha_{\text{curv}} = 0.1$, $\alpha_w = 80$, and $\alpha_n = 1 \times 10^{-5}$. PSNR values for f_{noise} and u^* are computed, and the standard deviations (STDs) of respective n^* are reported.

is captured by the w^* component, and it is well-separated from v^* . The n^* component corresponds to the noise whose STD is close to the true noise level. In the second row, we test the proposed model on a combination of silhouettes of ellipses and a circular wave of lighting. Under the nonuniform lighting, the ellipses are correctly identified in v^* and filled with nearly constant intensity. The w^* component shows the correct wave pattern of the lighting. In the third row, we have a shaded globe, where the source of the light is fixed at the top left corner. The proposed method correctly assigns in the v^* component the silhouettes of the globe with sharp boundaries. Noticeably, the proposed model keeps the soft shadow characterizing the volumetric feature of a ball in the w^* component with the correct direction of lighting. In the last row, we have a challenging case where a binarized portrait of Einstein is blended with

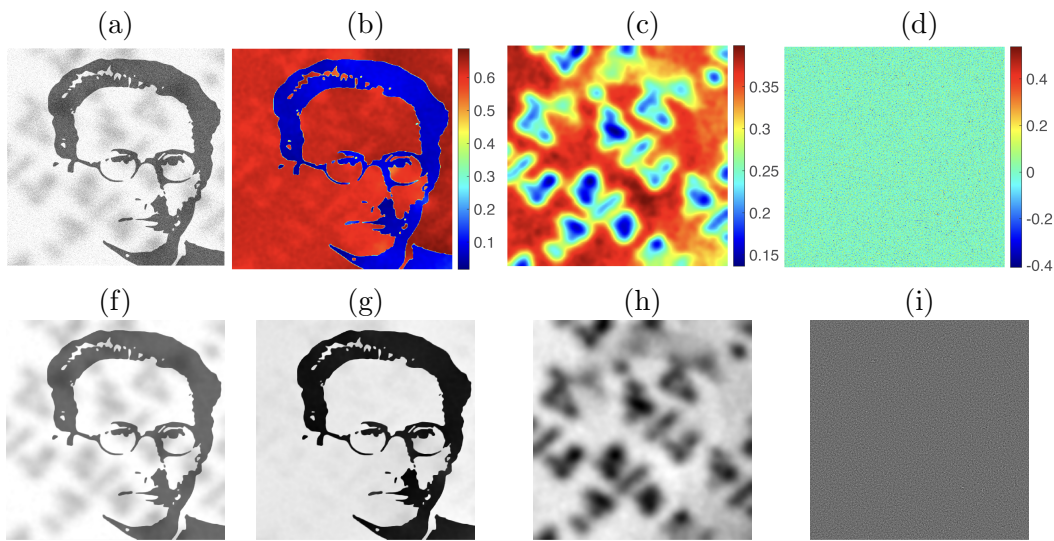


Figure 4. Illustration of the proposed method without scaling the components. (a) Input noisy image ($\sigma = 20/255$). (b) Identified structure component v^* . (c) Identified smooth component w^* . (d) Identified noise component n^* . (e) The reconstructed u^* component ($PSNR = 36.05$). (f)–(i) are the scaled versions of (b)–(d), respectively. The proposed method successfully separates visually distinctive components. Noticeably, n^* in (d) captures only unstructured oscillations ($STD = 19.77/255$).

multiple blurry shades of the mass-energy equation. The w^* component is more complicated than those in the previous examples. Our method successfully extracts the soft contents with complex shapes and leaves a relatively clean configuration for the v^* component.

To further examine the identified components by our method, we show in Figure 4 the decomposition results without scaling. In Figure 4(a), we show the noisy input image ($\sigma = 20/255$) where shadows of Schrödinger equations are cast over a binary portrait of Erwin Schrödinger. In Figure 4(b)–(d), we present the identified structure v^* , smooth part w^* , and oscillatory part n^* , respectively, without scaling. In Figure 4(f), we show the reconstructed u^* of the proposed method; and in Figure 4(g)–(i), we show the scaled versions of Figure 4(b)–(d), respectively. The ranges of the values confirm that the identified variations are substantial in Figure 4(b) and (c), and n^* in Figure 4(d) captures unstructured oscillations whose STD $19.77/255$ is close to the true one.

In Figure 5, we apply the proposed model to photorealistic grayscale images. In all examples, we observe that contents with sharp boundaries are captured by v^* , soft shadows and illumination variation are modeled by w^* , and the n^* keeps fine textures plus noise. Noticeably, in the first row, the rectangular reflectances on the dome are separated from the soft light and shadow defining the volume of the dome. In the second row, the foreground with crisp boundaries is distinguished from the background with blurry shapes.

The examples in Figure 3 and 5 justify the effectiveness of the proposed method. Thanks to the combination of the L^0 -gradient energy (2.3) and curvature regularization (2.4), the identified v^* component successfully preserves sharp structure boundaries while avoiding severe staircase effects. The extracted w^* component consistently matches the soft intensity

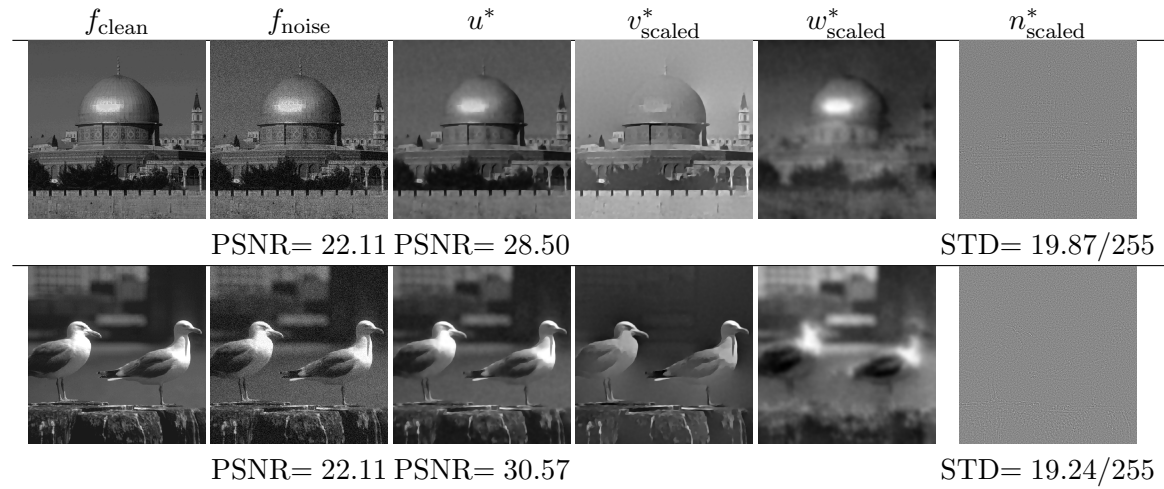


Figure 5. Decomposition of photographic images with noise ($\sigma = 20/255$). The first column (f_{clean}) shows the clean images; the second column (f_{noise}) shows the noisy inputs; the third column (u^*) shows summations of the identified v^* and w^* components; the subsequent columns show, respectively, v^* , w^* , and n^* , and for visualization, they are linearly scaled between 0 and 1. Model parameters for these examples are $\alpha_0 = 2 \times 10^{-3}$, $\alpha_{\text{curv}} = 0.5$, $\alpha_w = 50$, and $\alpha_n = 0.1$. PSNR values for f_{noise} and u^* are computed, and the STDs of respective n^* are reported.

variation caused by lighting and shadows. The extracted n^* component holds the oscillatory residuals including noise and fine-scale textures. We note that, when the input images do not contain rich textures, the n^* components rendered by the proposed model do not contain structural details such as boundaries. It allows us to use the summation of v^* and w^* , which is denoted by u^* , to reconstruct the clean image. This is justified by the PSNR values reported in Figure 3 and 5. Moreover, for general real images, since smooth transition is not necessarily uniform in the whole domain and w^* , by construction, does not allow discontinuous gradients, the structure component v^* is not strictly piecewise constant. Consequently, unnatural staircase effects may appear when applying L^0 -gradient regularization alone. With the curvature regularization in our proposed model, mild transition is allowed in v^* (see Remark 2.3), thus ameliorating the artifact. We further elaborate this in the next experiments.

5.2. Ablation study. To justify the combination of regularizations in our model (2.1), we compare it with the following settings:

1. **Model I.** An image f is decomposed into two parts: cartoon part u^* and oscillatory part n^* .

$$(5.1) \quad \{u^*, n^*\} = \arg \min_{u, n} \left[\alpha_0 \|\nabla u\|_0 + \alpha_n \|n\|_{H^{-1}(\Omega)}^2 + \frac{1}{2} \int_{\Omega} |f - (u + n)|^2 d\mathbf{x} \right].$$

2. **Model II.** An image f is decomposed into three parts: cartoon part v^* , smooth part w^* , and oscillatory part n^* .

$$(5.2) \quad \begin{aligned} \{v^*, w^*, n^*\} = \arg \min_{v, w, n} & \left[\alpha_0 \|\nabla v\|_0 + \alpha_w \|\Delta w\|_{L^2(\Omega)}^2 + \alpha_n \|n\|_{H^{-1}(\Omega)}^2 \right. \\ & \left. + \frac{1}{2} \int_{\Omega} |f - (v + w + n)|^2 d\mathbf{x} \right]. \end{aligned}$$

3. Model III. An image f is decomposed into two parts: homogeneous structure u^* and oscillatory part n^* .

$$(5.3) \quad \begin{aligned} \{u^*, n^*\} = \arg \min_{u, n} & \left[\alpha_0 \|\nabla u\|_0 + \alpha_{\text{curv}} \int_{\Omega} \left(\nabla \cdot \frac{\nabla u}{|\nabla u|} \right)^2 |\nabla u| d\mathbf{x} + \alpha_n \|n\|_{H^{-1}(\Omega)}^2 \right. \\ & \left. + \frac{1}{2} \int_{\Omega} |f - (u + n)|^2 d\mathbf{x} \right]. \end{aligned}$$

Compared to the proposed model, there is no smoothly varying component in Model I, and the regularity of u^* is mainly affected by the L^0 -gradient. In Model II, the noiseless component u^* is decomposed into a cartoon part v^* and a smooth part w^* , the same as in the proposed model, but there is no curvature regularization on v^* . In Model III, we impose both L^0 -gradient and curvature regularization on the noise-free approximation u^* , but there is no component that models the smooth shading.

Figure 6 shows the u^* components learned from the various settings above. In column (a), we present a noisy grayscale image of a squared ring, and the regions inside red boxes are zoomed-in and shown in the subsequent rows. We added Gaussian noise with intensity $\sigma = 50/255$ on the input. In column (b), we show the u^* component reconstructed by Model I (5.1). As was expected, using the regularization $\|\nabla u\|_0$ enforces strong sparsity on the gradient of reconstructed u^* component and yields sharp boundaries. However, analogous to the TV-norm regularization, using only the L^0 -gradient as regularization creates strong staircase effects. Moreover, the L^0 -gradient is local, yet larger-scale geometric information is necessary to render better results. The boundary in the third row shows undesirable irregularities. The smooth region is better reconstructed in Model II, where an extra component w^* is introduced. However, due to the lack of geometric information in the L^0 -gradient, the boundary lines still present zig-zags. In Model III, the curvature regularization on u^* is used, which imposes geometric priors on the level lines of v^* . The straight boundary lines are better preserved compared to Model I and Model II. Without the smooth part w^* , the intensity transition in the last row is not as smooth as in Model II. Combining the benefits of geometric regularization on the level lines and adding an extra smoothly varying component, our proposed model outperforms the others. Observe that the transition is smooth in the second row, as indicated by the red contour curves, and the boundary line is straight in the third row. These reconstructed features match the underlying image shown in the last column.

From this set of experiments, we conclude that L^0 -gradient regularization induces strong sparsity on the gradient, which causes significant staircase artifacts and irregular boundaries. These undesirable phenomena are effectively mitigated by the curvature regularization on the level lines. In order to recover smoothly varying regions while preserving sharp boundaries, our experiments show that adding an extra smooth part in the decomposition is important.

5.3. Effect of parameter α_w and α_{curv} . In our proposed model, both v^* and w^* favor regularity. Particularly, v^* prefers shapes with definite and regular boundaries, whereas w^*

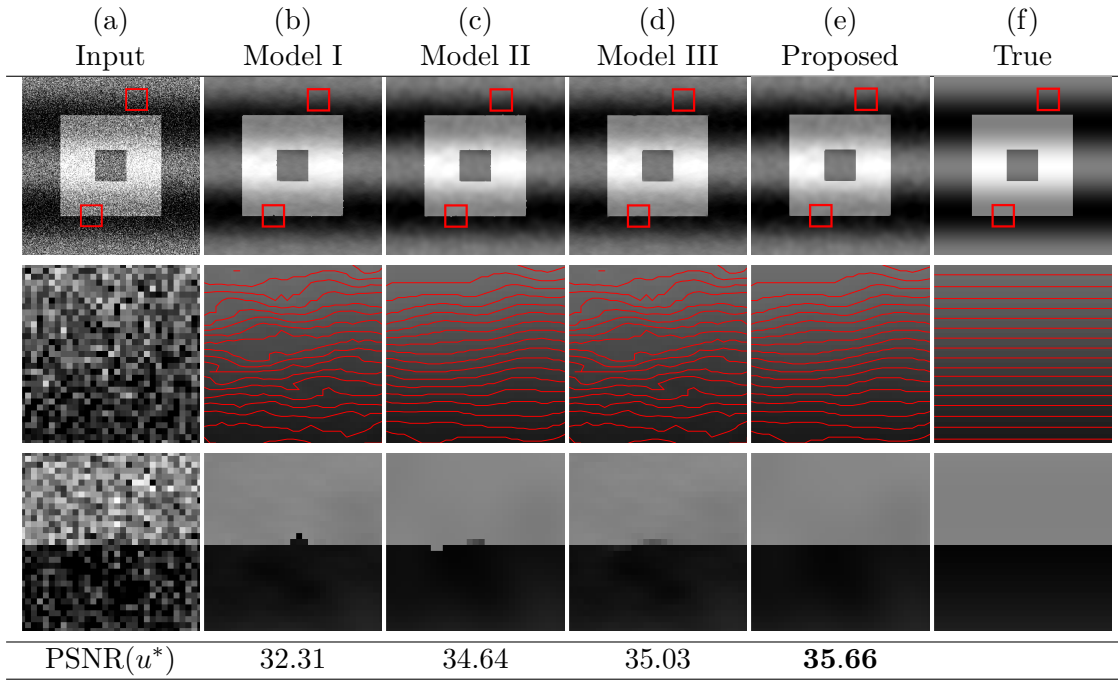


Figure 6. Ablation study. (a) Noisy input (size: 256×256 , $\sigma = 50/255$), and regions in red boxes are zoomed-in in the subsequent rows. (b) Noise-free component u^* by Model I (5.1), $\alpha_0 = 1.2 \times 10^{-1}$. (c) Noise-free component u^* by Model II (5.2), $\alpha_0 = 4 \times 10^{-2}$, $\alpha_w = 80$. (d) Noise-free component u^* by Model III (5.3), $\alpha_0 = 8 \times 10^{-2}$, $\alpha_{curv} = 2$. (e) Noise-free component u^* by the proposed model, $\alpha_0 = 5 \times 10^{-2}$, $\alpha_w = 80$, $\alpha_{curv} = 0.5$. (f) True image. For all scenarios, we fixed $\alpha_n = 1 \times 10^{-4}$. The noise-free components are obtained by summing the identified components except for the respective oscillatory parts.

tends to be blurry. We demonstrate that image content can be distributed and converted between these two components, yielding different decomposition results.

We first study the effect of the model parameter α_w associated with the term $\int_{\Omega} |\Delta w|^2 d\mathbf{x}$, which encourages isotropic smoothness of the w^* component. Intuitively, larger values of α_w induce smoother w^* where image details are smeared. If α_w is too large, regions with smoothly varying intensity and sufficiently regular level lines can be captured by the v^* component.

We illustrate this conversion between w^* and v^* affected by α_w in Figure 7. Given a noisy image ($\sigma = 10/255$), we apply the proposed model with α_w increasing from 10 to 1000 while fixing the other parameters. For each value of α_w , we show the scaled v^* and w^* components in the first and second row, respectively, and in the third row, we show the respective sum $u^* = v^* + w^*$. Observe that, with a wide range of values of α_w , the noise-free reconstruction u^* remains visually similar, and the PSNR values are stable. When α_w is small, most of the intensity variation is captured by w^* , while v^* only captures objects' large-scale contours. Although hair, face, eyes, and many recognizable shapes are visible in w^* , these distinct parts are blended with each other smoothly without sharp boundaries. As α_w increases, we see that w^* becomes more blurry and that v^* shows richer intensity variations such as those in the background. Note that these smoothly varying components in v^* have definite boundaries. For example, the zoom-ins of the red boxed region in the fourth row show that intensity

α_w	10	50	100	500	1000
v^* _{scaled}					
w^* _{scaled}					
u^*					
Zoom-in u^*					
PSNR(u^*)	34.58	34.59	34.53	34.34	34.28

Figure 7. Effect of α_w . When α_w increases, smooth intensity variations in w^* (second row) become structural shapes in v^* (first row): v^* contains richer details, e.g., the shades in the background, and w^* is more blurry. Overall, intensity transitions in u^* (third row) become sharper, which is further illustrated by the zoom-ins of the red box (fourth row). The input image Zelda is added with Gaussian noise ($\sigma = 10/255$). Other parameters are fixed: $\alpha_0 = 2 \times 10^{-3}$, $\alpha_{curv} = 0.5$, $\alpha_n = 10$.

transitions become sharper when α_w increases. Other softer smooth parts without distinctive boundaries, such as the shades on the cheeks and chin, are captured by the w^* component.

Second, we show the effect of the parameter α_{curv} , which is closely related to the regularity of the level lines in the v^* component. Similar to the previous study on the effect of α_w , by changing α_{curv} , smoothly varying components can transfer between w^* and v^* . In particular, if α_{curv} is large, certain regions with smooth intensity variation can be pushed into w^* for lower total loss.

Figure 8 presents results of the proposed model on a noisy image ($\sigma = 10/255$) with varying values of α_{curv} when the other regularization parameters are fixed. When α_{curv} increases from 0.01 to 10, we observe that the soft shades on the peppers in v^* are suppressed while the boundaries are preserved. Meanwhile, the w^* component gains more variation in the intensity. If we keep increasing α_{curv} above 0.1, the intensity variation near the boundaries and the highlights due to reflection slowly fade away in v^* . In contrast, the shapes of the peppers are more apparent in w^* . Since the sharp gradients in v^* are reduced and the intensity variation in w^* is intrinsically smooth, the reconstructed u^* component becomes slightly blurry.

α_{curv}	0.01	0.1	1	5	10
v^*_{scaled}					
w^*_{scaled}					
u^*					
Zoom-in u^*					
PSNR(u^*)	33.06	32.77	32.05	31.19	30.67

Figure 8. Effect of α_{curv} ($\sigma = 10/255$). When α_{curv} increases, v^* (first row) becomes smoother while objects' boundaries are preserved. The w^* component (second row) gains more geometric features such as shapes. Consequently, the sum u^* (third row) is smoother. Thanks to the curvature regularization, staircasing in the zoomed-in contours (last row) is effectively removed when increasing α_{curv} . Other parameters are fixed: $\alpha_0 = 2 \times 10^{-3}$, $\alpha_w = 50$, and $\alpha_n = 10$.

This transition is also reflected by the decreasing PSNR. In Figure 8, we also show the level lines of u^* in a zoomed-in region. The effect of α_{curv} on u^* is obvious. Increasing α_{curv} yields more regular level lines, and the staircase effect due to L^0 -gradient regularization is thus ameliorated.

5.4. Comparison on cartoon + smooth + oscillation decomposition. We compare the proposed model with models proposed by Chan, Esedoglu, and Park [14] (CEP) and Huska et al. [34] (HKLM), which are stated in (1.5) and (1.6), respectively. In both the proposed model and HKLM, an input image is decomposed into three components corresponding to cartoon-like part v^* , smooth part w^* , and oscillatory part n^* . For the four-component model (1.5), in addition to v^* and w^* , we take $n^* = n_1^* + n_2^*$; i.e., the oscillatory part is the summation of the texture and noise.

In Figure 9, we show the decomposition results from CEP, HKLM, and the proposed model when applied to a noisy synthetic image ($\sigma = 50/255$), respectively. For CEP [14] (see also (1.5)), we set $\lambda = 0.5$, $\alpha = 10$, $\mu = 2$ and the wavelet threshold δ is determined using Stein's unbiased risk estimate (SURE) [22]. For HKLM [34] (see also (1.6)), the authors proposed an

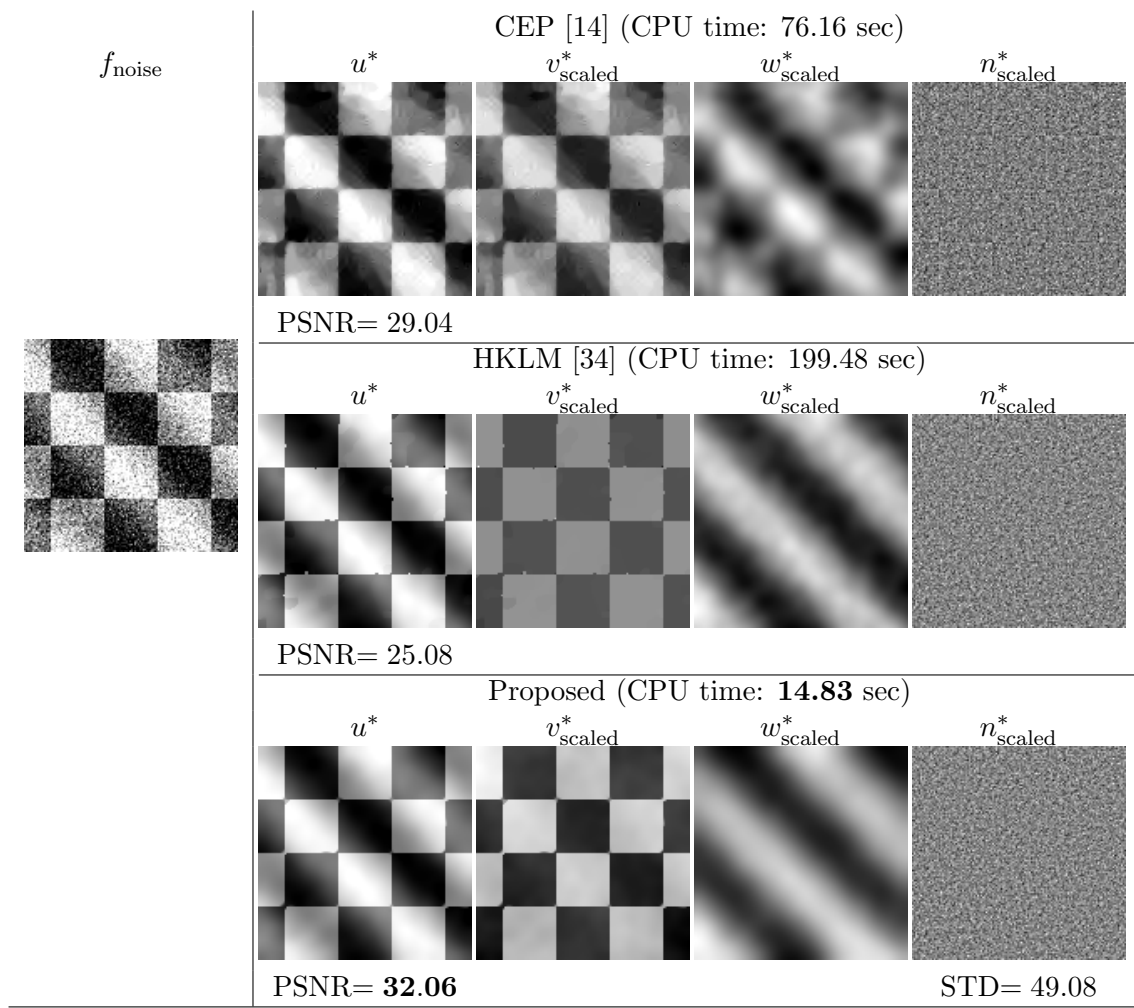


Figure 9. Comparison of Chan–Esedoglu–Park (CEP) [14], Huska–Kang–Lanza–Morigi (HKLM) [34], and the proposed model for decomposing a noisy synthetic image (size: 128×128 , noise: $\sigma = 50/255$). For CEP (see also (1.5)), we use $\lambda = 0.5, \alpha = 10, \mu = 2$, and δ determined by Stein unbiased risk estimate (SURE) [22]. For HKLM (see also (1.6)), we use $\beta_1 = 1 \times 10^{-4}, \beta_2 = 0.5, \beta_3 = 5 \times 10^{-6}$, and $a = 30$ for the MC penalty (an approximation of the L^0 -norm; see [34] for details). For the proposed model, we use $\alpha_0 = 4 \times 10^{-2}, \alpha_{\text{curv}} = 0.15, \alpha_w = 50$, and $\alpha_n = 1 \times 10^{-3}$.

automatic scheme for tuning the regularization parameters. However, we find that they fail to yield good decomposition results in general for our test images. To reach good PSNR values in u^* , after experimenting with different ranges of parameters, we manually set $\beta_1 = 1 \times 10^{-4}, \beta_2 = 0.5, \beta_3 = 5 \times 10^{-6}$, and the MC penalty (an approximation of the L^0 -norm; see [34] for details) parameter $a = 30$. For the proposed model, we use $\alpha_0 = 4 \times 10^{-2}, \alpha_{\text{curv}} = 0.15, \alpha_w = 50$ and $\alpha_n = 1 \times 10^{-3}$. We also present the summations of v^* and w^* as the noiseless approximations for f_{noise} and evaluate their respective PSNR values. In this example with heavy noise, both HKLM and our proposed model successfully separate the piecewise constant part from f_{noise} with strong sparsity of gradient thanks to the L^0 -gradient regularization, and

CEP with the TV-norm fails to produce a clean v^* part. Moreover, we observe that, with a heavy noise, regularization using only the L^0 -gradient as in HKLM yields irregular boundaries. In contrast, with the additional regularization on the curvature of level-set curves of v^* , our proposed model renders more satisfying results.

In Figure 10, we compare these methods using a grayscale photo of a butterfly with noise ($\sigma = 10/255$) and show the zoom-in comparisons in Figure 11. For CEP (see also (1.5)), we set $\lambda = 5$, $\alpha = 10$, $\mu = 2$, and δ determined from SURE [22]. For HKLM (see also (1.6)), we use $\beta_1 = 1 \times 10^{-4}$, $\beta_2 = 3$, $\beta_3 = 5 \times 10^{-6}$, and $a = 30$ for the MC penalty. For the proposed method, we use $\alpha_0 = 2 \times 10^{-3}$, $\alpha_{\text{curv}} = 0.05$, $\alpha_w = 30$, and $\alpha_n = 10$. All methods separate the structural part including patterns on the wing in the front, the smooth part including the blurry leaves in the back, as well as the oscillatory component such as noise. Compared to CEP, both HKLM and our proposed model produce better separations between the foreground details and background variations. Since HKLM uses only the L^0 -gradient for regularizing the v^* component, we observe that u^* of HKLM has the sharpest boundaries compared to CEP and the proposed model in Figure 11. This also yields irregular curves and strong staircase effects in Figure 11(d), which are effectively suppressed in CEP in (c) and the proposed model in Figure 11(e). Since CEP uses the TV-norm and the proposed model uses the stronger sparsity-inducing L^0 -gradient, the v^* component and consequently the u^* component resulting from the proposed model are clearer than those from CEP. Moreover, for this example, the noiseless approximation u^* produced by the proposed model has the highest PSNR value compared to the other two. We conclude that our proposed model produces more visually appealing decomposition results with better quality.

Our proposed model is also more efficient than CEP and HKLM. For the image of size 512×512 in Figure 10, CEP takes around 1655 s and HKLM takes over 4000 s, whereas our model only requires around 180 s. We note that HKLM requires to solve a dense linear system of size $(4NM) \times (4NM)$, which costs around $\mathcal{O}((NM)^3)$. As discussed in section 4, by leveraging FFT, the heaviest computation in our model requires solving a linear system of size 4×4 for each pixel in parallel, and the solution can be explicitly expressed. Overall, the computational cost of each iteration of our method is on the order or $\mathcal{O}(MN(\log M + \log N))$. This is similar for CEP, which involves both FFT and the discrete wavelet transform.

We note that the components identified by either HKLM or the proposed method may depend on the selected model parameters. In section D, we compare the proposed method with HKLM on results reported in the original paper using their fine-tuned parameters. In the next section, we study our model parameters in detail.

5.5. Selection of model parameters. There are four model parameters in the proposed model— α_0 , α_{curv} , α_w , and α_n —and it is generally difficult to determine their optimal values a priori. We demonstrate proper ranges for these model parameters that render good quality for u^* in terms of PSNR metric.

We take house, peppers, and blonde in Figure 12 with increasing levels of details. In the first set of experiments, we add Gaussian noise ($\sigma = 10/255$) and apply the proposed model to them with different combinations of α_{curv} and α_w while fixing $\alpha_0 = 2 \times 10^{-3}$ and $\alpha_n = 10$ from heuristics. Figure 13 shows the PSNR contours of the u^* components learned from the test images. We observe that, for $\alpha_w < 1$, the PSNR values are relatively low due to lack

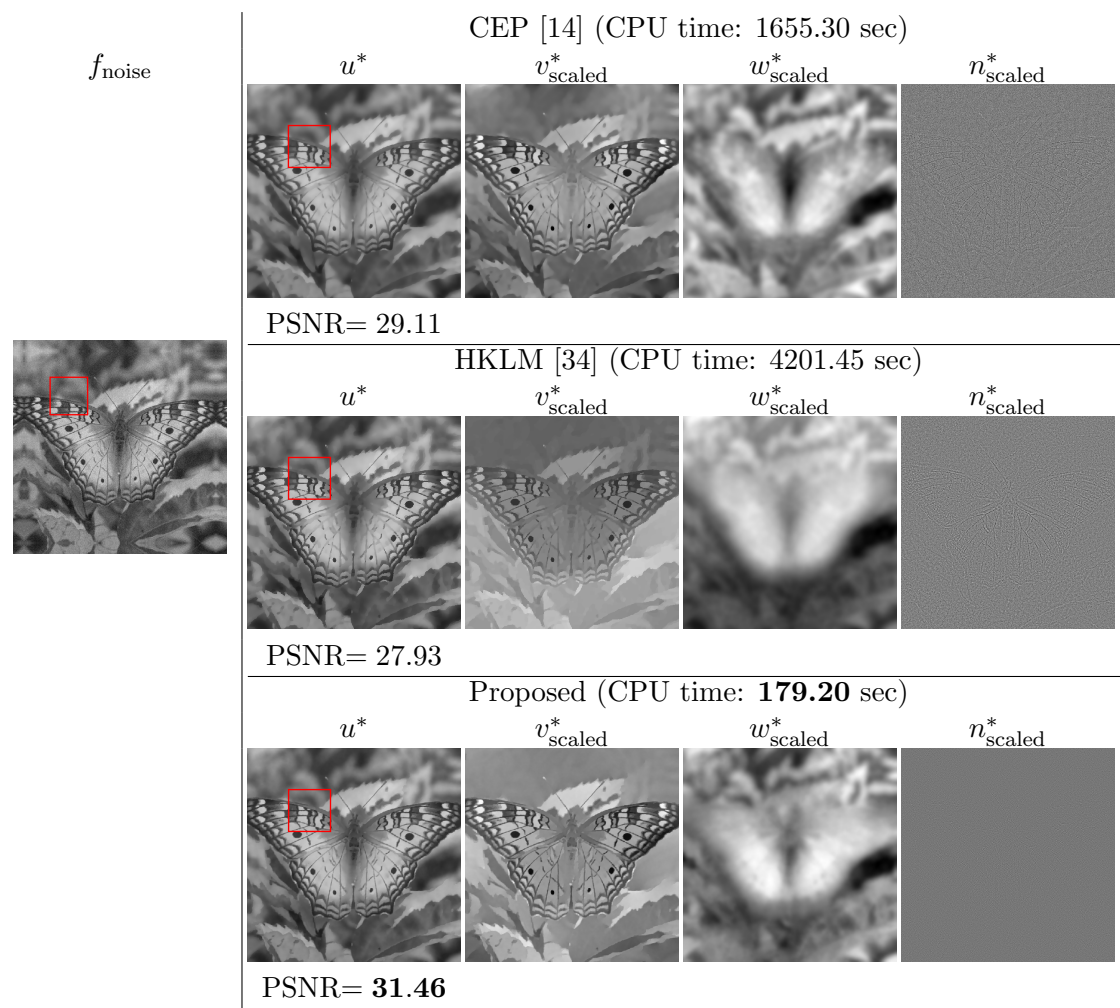


Figure 10. Comparison on cartoon + smooth + oscillation decomposition of CEP [14], HKLM [34], and the proposed model. f_{noise} is the input butterfly (size: 512×512 , noise: $\sigma = 10/255$). For CEP (see also (1.5)), we set $\lambda = 5$, $\alpha = 10$, $\mu = 2$, and δ determined from SURE [22]. For [34] (see also (1.6)), we use $\beta_1 = 1 \times 10^{-4}$, $\beta_2 = 3$, $\beta_3 = 5 \times 10^{-6}$, and $a = 30$ for the MC penalty. For the proposed model, we use $\alpha_0 = 2 \times 10^{-3}$, $\alpha_{\text{curv}} = 0.05$, $\alpha_w = 30$, and $\alpha_n = 10$.

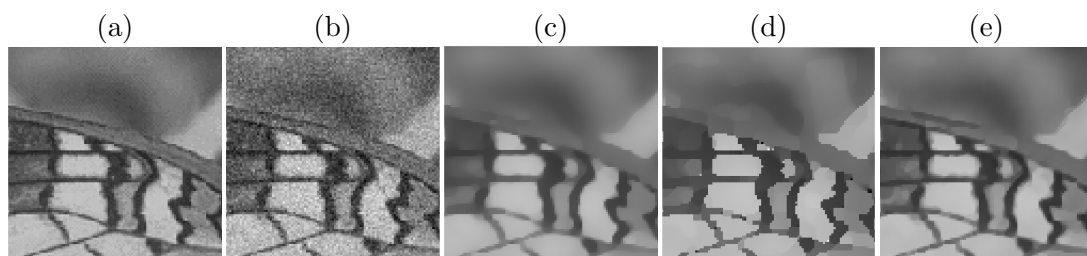


Figure 11. Zoom-ins of the boxed region in Figure 10. (a) Clean image. (b) Noisy input. (c) CEP [14]. (d) HKLM [34]. (e) Proposed.

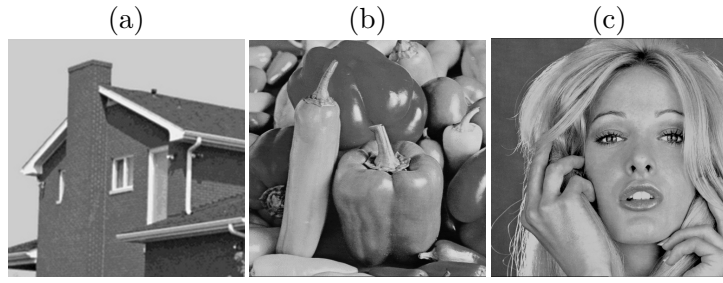


Figure 12. Images used for studying parameters in subsection 5.5. (a) House, (b) peppers, (c) blonde.

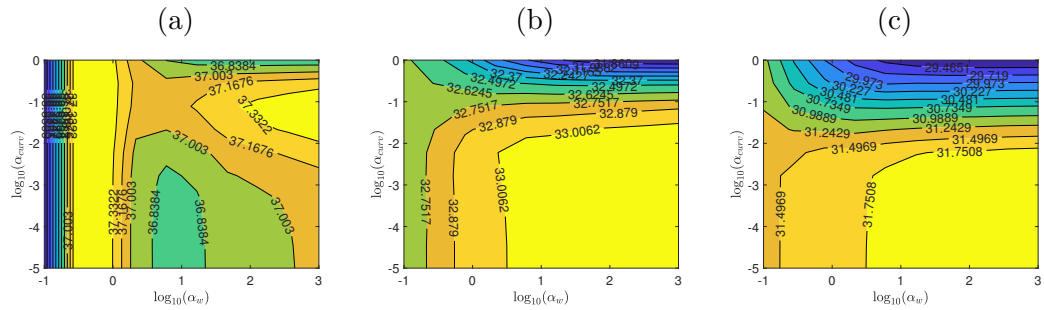


Figure 13. PSNR contour plots of u^* components generated by the proposed model for different combinations of α_{curv} and α_w . The inputs are (a) house, (b) peppers, and (c) blonde, which have increasing levels of details and textures. Images have Gaussian noise ($\sigma = 10/255$). Other parameters are fixed: $\alpha_0 = 2 \times 10^{-3}$, $\alpha_n = 10$. The parameter α_w is relatively stable when $\alpha_w \geq 1$. Choice of α_{curv} can depend on image contents. Higher values of α_{curv} are suitable for images with simple shapes and lower values for those with rich details.

of smoothness, and they increase as α_w grows. When $1 \leq \alpha_w \leq 10^3$, PSNR values become relatively insensitive to the choice of α_w . As for α_{curv} , we observe that the optimal values depend on image contents. Specifically, if the images are relatively simple, such as house, α_{curv} around $0.1 \sim 1$ yields slightly better quality. Because the images contain richer details such as those in peppers and blonde, the maximal PSNR values are obtained when α_{curv} takes smaller values around $10^{-3} \sim 10^{-2}$. We suggest fixing α_{curv} on the order of 0.1 and α_w on the order of 10. In case fine-tuning is needed, a proper range for α_{curv} is $10^{-3} \sim 1$, where smaller values are suitable for complex images, and larger values for simple ones. As for α_w , keeping it above 1 is a good practice. Investigations of their effects on the decomposition are collected in section 5.3.

We conduct our second set of experiments to search for appropriate α_n while fixing $\alpha_{curv} = 0.1$ and $\alpha_w = 50$. Since α_n is directly associated with the noise level, we show in Figure 14 the PSNR values of u^* components learned from test images by the proposed model, where both α_n and the noise level σ vary. We observe that, for noise levels below 20, the optimal choices of α_n stably remain around $0.1 \sim 10$. When the noise level grows above 20, we observe that the optimal choice of α_n has a clear dependence on σ . In particular, smaller α_n is needed for larger σ to capture oscillations due to noises. We could fit α_n in log-scale with $\sigma > 20$ using a quadratic polynomial; instead, we suggest a strategy for images with noise $\sigma < 100$ with better generalizability. We roughly divide the levels of noise into three regimes: low noise

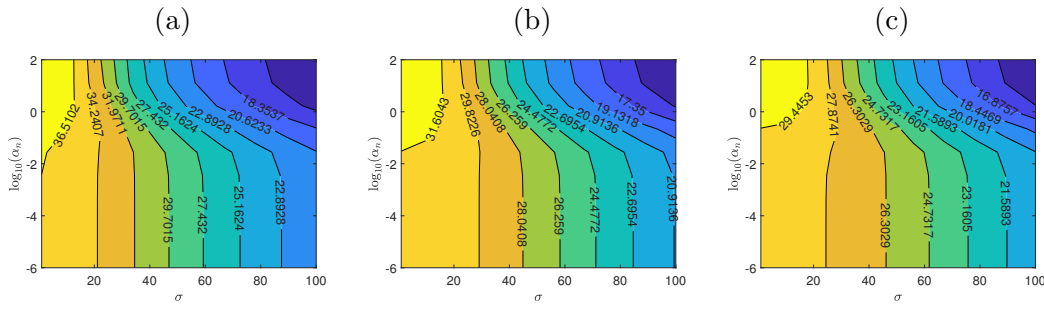


Figure 14. PSNR contour plots of u^* components generated by the proposed model for different values of α_n under various levels of noise σ . The inputs are (a) house, (b) peppers, and (c) blonde, which have increasing levels of details and textures. Other parameters are fixed: $\alpha_0 = 2 \times 10^{-3}$, $\alpha_{curv} = 0.1$, $\alpha_w = 50$. For low-noise regime ($\sigma < 20$), $\alpha_n \approx 1$ is appropriate; for middle levels of noise ($20 \leq \sigma < 60$), we suggest using $\alpha_n \approx 10^{-4}$; and for high-noise regime, $\alpha_n \approx 1 \times 10^{-6}$ is more suitable.

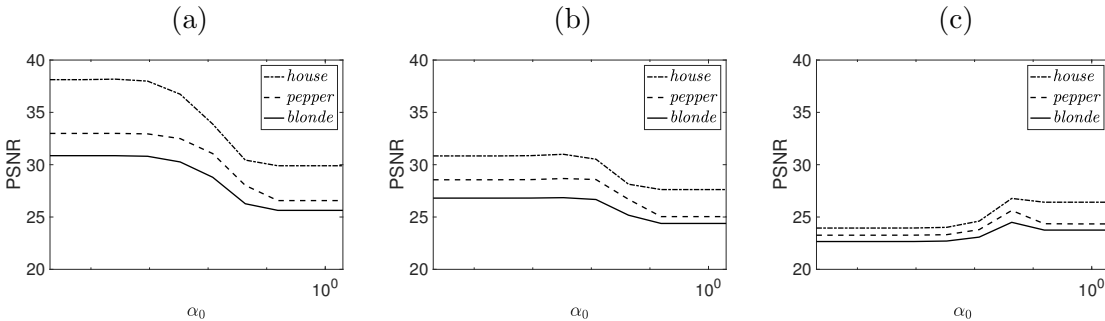


Figure 15. PSNR values of u^* components for noisy inputs with varying α_0 . (a) $\sigma = 10$, (b) $\sigma = 40$, (c) $\sigma = 80$. In these examples, $\alpha_{curv} = 0.1$, $\alpha_w = 50$. The parameter α_n is fixed at 10, 1×10^{-2} , and 1×10^{-4} , respectively.

($\sigma < 20$), medium noise ($20 \leq \sigma < 60$), and high noise ($60 \leq \sigma < 100$). For images with low noise, use $\alpha_n = 10$; for images with medium noise, use $\alpha_n = 1 \times 10^{-2}$; and for those with heavy noise, use $\alpha_n = 1 \times 10^{-4}$.

With α_{curv} , α_w , and α_n determined above, we proceed to tune α_0 . Using various values of α_0 , we record in Figure 15 the corresponding PSNR values of the u^* components for the three test images with different levels of noise. Specifically, we add Gaussian noises with $\sigma = 10/255$ in (a), $\sigma = 40/255$ in (b), and $\sigma = 80/255$ in (c). As discussed above, we use $\alpha_n = 10$ for (a), $\alpha_n = 1 \times 10^{-2}$ for (b), and $\alpha_n = 1 \times 10^{-4}$ for (c); and we fix $\alpha_{curv} = 0.1$ and $\alpha_w = 50$. For the tested images, when the noise is mild as in (a) and (b), we observe two plateaus in PSNR values of u^* components connected by decreasing phases between $2 \times 10^{-5} < \alpha_0 < 2$. The transitions from the high PSNR to low PSNR regime are smooth, and they correspond to removing rich image details such as textures. However, when the noise level is high as in (c), we observe that, as α_0 increases, the PSNR values improve slightly. This shows that the L^0 -gradient can contribute to perturbation reduction in a case with heavy noise. For general images, we suggest using $\alpha_0 = 2 \times 10^{-3}$ as the default.

6. Conclusion. In this paper, we propose a novel model for decomposing grayscale images into three components: the structural part, the smooth part, and the oscillatory part, each of which has a distinctive visual feature. To take advantage of the strong sparsity induced by the L^0 -gradient regularization while avoiding the undesirable staircase effect, our model integrates the curvature regularization on the level lines of the structural part. As a result, the reconstructed structural part effectively preserves sharp boundaries enclosing homogeneous regions. To solve the associated energy minimization problem, we develop an efficient numerical algorithm based on operator splitting. The original nonconvex nonsmooth problem is separated into four subproblems. Each of them either admits a closed-form solution or enjoys a form suitable for applying FFT. We present various experiments to justify the proposed model. In particular, we show that our model successfully separates underlying patterns from soft shadows even when both of them have complicated geometries with fine details. We also justify the regularization terms included in the proposed model and illustrate the effects of parameters. We compare our model with CEP [14] and HKLM [34] for three-component decomposition and show that our model achieves visually appealing results and outstanding computational efficiency. To amend the loss of fine-scale details, a natural extension is to model noise and textures separately. The proposed method can also be extended to color image decomposition when applied channelwise. To avoid potential artifacts, we leave it as a future work to investigate appropriate regularizers that leverage correlations among color channels.

Appendix A. Proof of Proposition 2.1.

Proof. The proof is analogous to [20]. Denote

$$\begin{aligned} E_1(v, w, n) &= \alpha_0 L_G^0(v) + \alpha_{\text{curv}} \int_{\Omega} \kappa^2(v) |\nabla v| + \alpha_w \|\Delta w\|_{L^2(\Omega)}^2 + \alpha_n \|n\|_{H^{-1}(\Omega)}^2, \\ E_2(v, w, n) &= \frac{1}{2} \int_{\Omega} |f - (v + w + n)|_2^2 d\mathbf{x}. \end{aligned}$$

Let (v^*, w^*, n^*) be a minimizer of model (2.7). Consider the tuple $(v^* + c_1, w^* + c_2, n^*)$, where $c_1, c_2 \in \mathbb{R}$ are scalar fields. Notice that

$$E_1(v^*, w^*, n^*) = E_1(v^* + c_1, w^* + c_2, n^*)$$

and

$$\begin{aligned} E_2(v^* + c_1, w^* + c_2, n^*) &= \frac{1}{2} \int_{\Omega} |f - (v^* + c_1 + w^* + c_2 + n^*)|^2 d\mathbf{x} \\ (A.1) \quad &= E_2(v^*, w^*, n^*) + (c_1 + c_2) \int_{\Omega} (v^* + w^* + n^* - f) d\mathbf{x} + \frac{|\Omega|}{2} (c_1 + c_2)^2, \end{aligned}$$

where $|\Omega|$ is the area of Ω . The function on the right-hand side of (A.1) is quadratic in $(c_1 + c_2)$, which takes its minimal value $E_2(v^*, w^*, n^*) - (2|\Omega|)^{-1} (\int_{\Omega} (f - (v^* + w^* + n^*)) d\mathbf{x})^2$ when

$$(A.2) \quad c_1 + c_2 = \frac{\int_{\Omega} (f - (v^* + w^* + n^*)) d\mathbf{x}}{|\Omega|}.$$

If $\int_{\Omega}(f - (v^* + w^* + n^*))d\mathbf{x} \neq 0$ for any c_1 and c_2 that satisfy (A.2), it would imply that

$$\begin{aligned} & E_1(v^*, w^*, n^*) + E_2(v^*, w^*, n^*) \\ & > E_1(v^*, w^*, n^*) + E_2(v^*, w^*, n^*) - (2|\Omega|)^{-1} \left(\int_{\Omega}(f - (v^* + w^* + n^*))d\mathbf{x} \right)^2 \\ & = E_1(u^* + c_1, w^* + c_2, n^*) + E_2(u^* + c_1, w^* + c_2, n^*), \end{aligned}$$

which contradicts the assumption that (v^*, w^*, n^*) is a minimizer of model (2.7). We thus conclude that $\int_{\Omega} v^* + w^* + n^* d\mathbf{x} = \int_{\Omega} f d\mathbf{x}$. ■

Appendix B. Equivalence between Hessian and Laplacian regularizer.

We compare

$$E_H(w) = \frac{1}{2} \|\partial^2 w\|_{L^2(\Omega)}^2 \quad \text{with} \quad E_L(w) = \frac{1}{2} \|\Delta w\|_{L^2(\Omega)}^2.$$

Functional E_H is used in [34], and E_L is used in this paper as a regularizer for the w component. It was observed in [14] that $E_H = E_L$ for compactly supported smooth functions. We show that more general boundary conditions E_H and E_L have the same set of critical points. To prove that, it is sufficient to show that their variations concerning w have the same form. For simplicity, we assume that $\Omega = [0, L_1] \times [0, L_2]$ for some $L_1, L_2 > 0$.

The functional E_H can be written as

$$E_H(w) = \frac{1}{2} \int_{\Omega} \left(\frac{\partial^2 w}{\partial x_1^2} \right)^2 + 2 \left(\frac{\partial^2 w}{\partial x_1 \partial x_2} \right)^2 + \left(\frac{\partial^2 w}{\partial x_2^2} \right)^2 d\mathbf{x}.$$

The Fréchet derivative of E_H with respect to w in the direction h is

$$\begin{aligned} \left\langle \frac{\partial E_H}{\partial w}, h \right\rangle &= \int_{\Omega} \left(\frac{\partial^4 w}{\partial x_1^4} + 2 \frac{\partial^4 w}{\partial x_1^2 \partial x_2^2} + \frac{\partial^4 w}{\partial x_2^4} \right) h d\mathbf{x} \\ &\quad - \left\langle \frac{\partial^2 w}{\partial x_1^2}, \frac{\partial h}{\partial x_1} \right\rangle \Big|_{x_1=0}^{x_1=L_1} + \left\langle \frac{\partial^3 w}{\partial x_1^3}, h \right\rangle \Big|_{x_1=0}^{x_1=L_1} \\ &\quad - \left\langle \frac{\partial^2 w}{\partial x_2^2}, \frac{\partial h}{\partial x_2} \right\rangle \Big|_{x_2=0}^{x_2=L_2} + \left\langle \frac{\partial^3 w}{\partial x_2^3}, h \right\rangle \Big|_{x_2=0}^{x_2=L_2} \\ &\quad - \left\langle \frac{\partial^2 w}{\partial x_1 \partial x_2}, \frac{\partial h}{\partial x_2} \right\rangle \Big|_{x_1=0}^{x_1=L_1} + \left\langle \frac{\partial^3 w}{\partial x_1^2 \partial x_2}, h \right\rangle \Big|_{x_2=0}^{x_2=L_2} \\ (B.1) \quad &\quad - \left\langle \frac{\partial^2 w}{\partial x_1 \partial x_2}, \frac{\partial h}{\partial x_1} \right\rangle \Big|_{x_2=0}^{x_2=L_2} + \left\langle \frac{\partial^3 w}{\partial x_1 \partial x_2^2}, h \right\rangle \Big|_{x_1=0}^{x_1=L_1}. \end{aligned}$$

The functional E_L can be written as

$$E_L(w) = \frac{1}{2} \int_{\Omega} \left(\frac{\partial^2 w}{\partial x_1^2} \right)^2 + 2 \left(\frac{\partial^2 w}{\partial x_1^2} \frac{\partial^2 w}{\partial x_2^2} \right) + \left(\frac{\partial^2 w}{\partial x_2^2} \right)^2 d\mathbf{x}.$$

The Fréchet derivative of E_L with respect to w in the direction h is

$$(B.2) \quad \begin{aligned} \left\langle \frac{\partial E_L}{\partial w}, h \right\rangle &= \int_{\Omega} \left(\frac{\partial^4 w}{\partial x_1^4} + 2 \frac{\partial^4 w}{\partial x_1^2 \partial x_2^2} + \frac{\partial^4 w}{\partial x_2^4} \right) h \, d\mathbf{x} \\ &\quad - \left\langle \left(\frac{\partial^2 w}{\partial x_1^2} + \frac{\partial^2 w}{\partial x_2^2} \right), \frac{\partial h}{\partial x_1} \right\rangle \Big|_{x_1=0}^{x_1=L_1} + \left\langle \left(\frac{\partial^3 w}{\partial x_1^3} + \frac{\partial^3 w}{\partial x_1^2 \partial x_2} \right), h \right\rangle \Big|_{x_1=0}^{x_1=L_1} \\ &\quad - \left\langle \left(\frac{\partial^2 w}{\partial x_2^2} + \frac{\partial^2 w}{\partial x_1^2} \right), \frac{\partial h}{\partial x_2} \right\rangle \Big|_{x_2=0}^{x_2=L_2} + \left\langle \left(\frac{\partial^3 w}{\partial x_2^3} + \frac{\partial^3 w}{\partial x_1 \partial x_2^2} \right), h \right\rangle \Big|_{x_2=0}^{x_2=L_2}. \end{aligned}$$

By using the boundary condition

$$\frac{\partial^2 w}{\partial x_1^2} = \frac{\partial^2 w}{\partial x_2^2} = \frac{\partial^3 w}{\partial x_1^3} = \frac{\partial^3 w}{\partial x_2^3} = \frac{\partial^3 w}{\partial x_1^2 \partial x_2} = \frac{\partial^3 w}{\partial x_1 \partial x_2^2} = 0 \text{ on } \partial\Omega,$$

all boundary integrals in (B.1) and (B.2) vanish. We get the same Fréchet derivative for both E_H and E_L :

$$\left\langle \frac{\partial E_H}{\partial w}, h \right\rangle = \left\langle \frac{\partial E_L}{\partial w}, h \right\rangle = \int_{\Omega} \left(\frac{\partial^4 w}{\partial x_1^4} + 2 \frac{\partial^4 w}{\partial x_1^2 \partial x_2^2} + \frac{\partial^4 w}{\partial x_2^4} \right) h \, d\mathbf{x}.$$

Therefore, E_H and E_L have the same optimality condition and thus the same set of critical points.

Appendix C. Details on adapting to periodic boundary conditions. Without loss of generality, consider a rectangular domain $\Omega = [0, L_1] \times [0, L_2]$, and define the spaces

$$(C.1) \quad H_P^k(\Omega) = \{v \in H^k(\Omega) : v(0, y) = v(L_1, y), v(:, 0) = v(:, L_2)\}$$

for $k = 1, 2$. We revise the set Σ_f to

$$(C.2) \quad \Sigma_f = \left\{ (\mathbf{q}, w, \mathbf{g}) \in (L^2(\Omega))^2 \times L^2(\Omega) \times (H^1(\Omega))^2 \mid \exists v \in H_P^1(\Omega) \text{ such that } \mathbf{q} = \nabla v \text{ and } \int_{\Omega} (v + w + \nabla \cdot \mathbf{g} - f) \, d\mathbf{x} = 0 \right\}.$$

Problem (2.12) and (2.10) are replaced by

$$(C.3) \quad \begin{aligned} &\min_{\substack{\mathbf{q} \in (H_P^1(\Omega))^2, \boldsymbol{\mu} \in (H_P^1(\Omega))^2, \\ w \in H_P^2(\Omega), \mathbf{g} \in (H_P^1(\Omega))^2}} \left[\alpha_0 \int_{\Omega} \|\mathbf{q}\|_0 \, d\mathbf{x} + \alpha_{\text{curv}} \int_{\Omega} |\nabla \cdot \boldsymbol{\mu}|^2 |\mathbf{q}| \, d\mathbf{x} + \alpha_w \int_{\Omega} |\Delta w|^2 \, d\mathbf{x} \right. \\ &\quad \left. + \alpha_n \int_{\Omega} |\mathbf{g}|^2 \, d\mathbf{x} + \frac{1}{2} \int_{\Omega} |f - (v_{\mathbf{q}} + w + \nabla \cdot \mathbf{g})|^2 \, d\mathbf{x} + I_{\Sigma_f}(\mathbf{q}, w, \mathbf{g}) + I_S(\mathbf{q}, \boldsymbol{\mu}) \right] \end{aligned}$$

and

$$(C.4) \quad \begin{cases} \Delta v_{\mathbf{q}, w, \mathbf{g}} = \nabla \cdot \mathbf{q} & \text{in } \Omega, \\ \int_{\Omega} v_{\mathbf{q}, w, \mathbf{g}} d\mathbf{x} = \int_{\Omega} f - w - \nabla \cdot \mathbf{g} d\mathbf{x}, \\ v_{\mathbf{q}, w, \mathbf{g}}(0, x_2) = v_{\mathbf{q}, w, \mathbf{g}}(L_1, x_2) & \text{for } 0 \leq x_2 \leq L_2, \\ v_{\mathbf{q}, w, \mathbf{g}}(x_1, 0) = v_{\mathbf{q}, w, \mathbf{g}}(x_1, L_2) & \text{for } 0 \leq x_1 \leq L_1, \\ \left(\frac{\partial v_{\mathbf{q}, w, \mathbf{g}}}{\partial x_1} - q_1 \right)(0, x_2) = \left(\frac{\partial v_{\mathbf{q}, w, \mathbf{g}}}{\partial x_1} - q_1 \right)(L_1, x_2) & \text{for } 0 \leq x_2 \leq L_2, \\ \left(\frac{\partial v_{\mathbf{q}, w, \mathbf{g}}}{\partial x_2} - q_2 \right)(x_1, 0) = \left(\frac{\partial v_{\mathbf{q}, w, \mathbf{g}}}{\partial x_2} - q_2 \right)(x_1, L_2) & \text{for } 0 \leq x_1 \leq L_1. \end{cases}$$

For subproblem solvers, we replace (3.10) and (3.11) by

$$(C.5) \quad \boldsymbol{\lambda}^{k+2/4} = \arg \min_{\boldsymbol{\mu} \in (H_P^1(\Omega))^2} \left[\frac{\gamma_1}{2} \int_{\Omega} |\boldsymbol{\mu} - \boldsymbol{\lambda}^{k+1/4}|^2 d\mathbf{x} + \tau \alpha_w \int_{\Omega} |\nabla \cdot \boldsymbol{\mu}|^2 |\mathbf{p}^{k+2/4}| d\mathbf{x} \right]$$

and

$$(C.6) \quad \begin{cases} \gamma_1 \frac{\boldsymbol{\lambda}^{k+2/4} - \boldsymbol{\lambda}^{k+1/4}}{\tau} - 2\alpha_w \nabla(|\mathbf{p}^{k+2/4}| \nabla \cdot \boldsymbol{\lambda}^{k+2/4}) = 0 & \text{in } \Omega, \\ (|\mathbf{p}^{k+2/4}| \nabla \cdot \boldsymbol{\lambda}^{k+2/4})(0, x_2) = (|\mathbf{p}^{k+2/4}| \nabla \cdot \boldsymbol{\lambda}^{k+2/4})(L_1, x_2) & \text{for } 0 \leq x_2 \leq L_2, \\ (|\mathbf{p}^{k+2/4}| \nabla \cdot \boldsymbol{\lambda}^{k+2/4})(x_1, 0) = (|\mathbf{p}^{k+2/4}| \nabla \cdot \boldsymbol{\lambda}^{k+2/4})(x_1, L_1) & \text{for } 0 \leq x_1 \leq L_1, \end{cases}$$

respectively.

Replace (3.23), (3.24), and (3.25) by

$$(C.7) \quad \begin{aligned} & \min_{\substack{(\mathbf{q}, w, \mathbf{g}) \in \Sigma_f, w \in H_P^2(\Omega), \\ \mathbf{g} \in (H_P^1(\Omega))^2}} \left[\frac{1}{2} \int_{\Omega} |\mathbf{q} - \mathbf{p}^{k+3/4}|^2 d\mathbf{x} + \frac{\gamma_2}{2} \int_{\Omega} |w - r^{k+3/4}|^2 d\mathbf{x} + \frac{\gamma_3}{2} \int_{\Omega} |\mathbf{g} - \mathbf{s}^{k+3/4}|^2 d\mathbf{x} \right. \\ & \quad \left. + \tau \alpha_w \int_{\Omega} |\Delta w|^2 d\mathbf{x} + \tau \alpha_n \int_{\Omega} |\mathbf{g}|^2 d\mathbf{x} + \frac{\tau}{2} \int_{\Omega} |f - (v_{\mathbf{q}, w, \mathbf{g}} + w + \nabla \cdot \mathbf{g})|^2 d\mathbf{x} \right], \end{aligned}$$

$$(C.8) \quad \begin{cases} (v^{k+1}, r^{k+1}, \mathbf{s}^{k+1}) = \arg \min_{\substack{v \in H_P^1(\Omega), w \in H_P^2(\Omega), \\ \mathbf{g} \in (H_P^1(\Omega))^2}} \left[\frac{1}{2} \int_{\Omega} |\nabla v - \mathbf{p}^{k+3/4}|^2 d\mathbf{x} + \frac{\gamma_2}{2} \int_{\Omega} |w - r^{k+3/4}|^2 d\mathbf{x} \right. \\ \quad \left. + \frac{\gamma_3}{2} \int_{\Omega} |\mathbf{g} - \mathbf{s}^{k+3/4}|^2 d\mathbf{x} + \tau \alpha_w \int_{\Omega} |\Delta w|^2 d\mathbf{x} + \tau \alpha_n \int_{\Omega} |\mathbf{g}|^2 d\mathbf{x} \right. \\ \quad \left. + \frac{\tau}{2} \int_{\Omega} |f - (v + w + \nabla \cdot \mathbf{g})|^2 d\mathbf{x} \right], \\ \mathbf{p}^{k+1} = \nabla v^{k+1}, \end{cases}$$

and

(C.9)

$$\left\{ \begin{array}{l} \frac{-\Delta v^{k+1} + \nabla \cdot \mathbf{p}^{k+3/4}}{\tau} + v^{k+1} - (f - r^{k+1} - \nabla \cdot \mathbf{s}^{k+1}) = 0, \\ \left(\frac{\partial v^{k+1}}{\partial x_1} - p_1^{k+3/4} \right) (0, x_2) = \left(\frac{\partial v^{k+1}}{\partial x_1} - p_1^{k+3/4} \right) (L_1, x_2), \\ \left(\frac{\partial v^{k+1}}{\partial x_2} - p_2^{k+3/4} \right) (x_1, 0) = \left(\frac{\partial v^{k+1}}{\partial x_2} - p_2^{k+3/4} \right) (x_1, L_2), \\ \gamma_2 \frac{r^{k+1} - r^{k+3/4}}{\tau} + r^{k+1} - (f - v^{k+1} - \nabla \cdot \mathbf{s}^{k+1}) + 2\alpha_w (\nabla^4 r^{k+1}) = 0, \\ (\Delta r^{k+1})(0, x_2) = (\Delta r^{k+1})(L_1, x_2), \quad \left(\frac{\partial (\Delta r^{k+1})}{\partial x_1} \right) (0, x_2) = \left(\frac{\partial (\Delta r^{k+1})}{\partial x_1} \right) (L_1, x_2), \\ (\Delta r^{k+1})(x_1, 0) = (\Delta r^{k+1})(x_1, L_2), \quad \left(\frac{\partial (\Delta r^{k+1})}{\partial x_2} \right) (x_1, 0) = \left(\frac{\partial (\Delta r^{k+1})}{\partial x_2} \right) (x_1, L_2), \\ \gamma_3 \frac{\mathbf{s}^{k+1} - \mathbf{s}^{k+3/4}}{\tau} - \nabla (\nabla \cdot \mathbf{s}^{k+1}) + 2\alpha_n \mathbf{s}^{k+1} + \nabla (f - v^{k+1} - r^{k+1}) = 0, \\ (f - (v^{k+1} + r^{k+1} + \nabla \cdot \mathbf{s}^{k+1})) (0, x_2) = (f - (v^{k+1} + r^{k+1} + \nabla \cdot \mathbf{s}^{k+1})) (L_1, x_2), \\ (f - (v^{k+1} + r^{k+1} + \nabla \cdot \mathbf{s}^{k+1})) (x_1, 0) = (f - (v^{k+1} + r^{k+1} + \nabla \cdot \mathbf{s}^{k+1})) (x_1, L_2), \end{array} \right.$$

respectively, with $\mathbf{p} = (p_1, p_2)$ and $0 \leq x_1 \leq L_1, 0 \leq x_2 \leq L_2$.

Appendix D. Further comparisons with HKLM [34]. We compare with the original results in Figure 6.8 of [34]. Figure 16(a) shows the input image; in the second row, Figure 16(b) shows the reconstructed oscillation-free part u_{HKLM}^* ; Figure 16(c) shows the structure (or car-

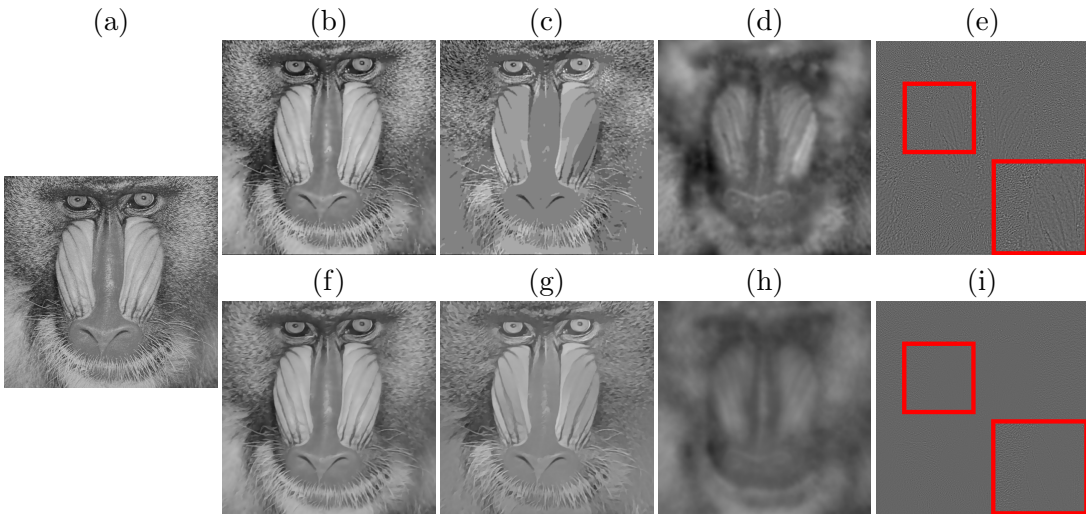


Figure 16. Comparison with results in Figure 6.8 in [34] by HKLM. (a) The input clean image. (b)–(e) show the results from HKLM: (b) u_{HKLM}^* , (c) v_{HKLM}^* , (d) $w_{HKLM}^* + 0.4$, and (e) $2n_{HKLM}^* + 0.4$. (f)–(i) show the results by the proposed method using the default parameters: (f) $u_{proposed}^*$, (g) $v_{proposed}^*$, (h) $w_{proposed}^* + 0.4$, and (i) $2n_{proposed}^* + 0.4$. The scaling and shifting on the intensity values follow those used in [34].

toon) part v_{HKLM}^* ; Figure 16(d) shows the shifted smooth part $w_{\text{HKLM}}^* + 0.4$; and Figure 16(e) shows the transformed oscillatory part $2n_{\text{HKLM}}^* + 0.4$. Following the same transformations, in the second row, we show the counterparts by our method in Figure 16(f)–(i), respectively. We use the default model parameters as those in Figure 5. We observe that both methods yield similar oscillation-free part, as shown in Figure 16(b) and (f). For the structure part, our result in Figure 16(g) shows less staircase effect than Figure 16(c). For the smooth part, our result in Figure 16(h) captures soft transitions of the shadows while avoiding pattern boundaries on the face in Figure 16(d). For the oscillatory part, our result in Figure 16(i) contains overall weaker variations compared to Figure 16(e); our textures mostly concentrate around the furry region, whereas the pattern boundaries in Figure 16(e) are retained. See the zoom-in boxes.

Acknowledgments. We would like to thank Dr. Martin Huska at University of Bologna for kindly sharing the code of [34]. We would also like to thank Prof. Sung Ha Kang at Georgia Institute of Technology for inspiring discussions on high-order regularizations.

REFERENCES

- [1] L. AMBROSIO AND S. MASNOU, *A direct variational approach to a problem arising in image reconstruction*, Interface. Free Bound., 5 (2003), pp. 63–81, <https://doi.org/10.4171/ifb/72>.
- [2] G. ANZELLOTTI, *Pairings between measures and bounded functions and compensated compactness*, Ann. Mat. Pura Appl., 135 (1983), pp. 293–318, <https://doi.org/10.1007/BF01781073>.
- [3] D. N. ARNOLD, R. S. FALK, AND R. WINTHER, *Multigrid in $H(\text{div})$ and $H(\text{curl})$* , Numer. Math., 85 (2000), pp. 197–217, <https://doi.org/10.1007/PL000005386>.
- [4] G. AUBERT AND J.-F. AUJOL, *Modeling very oscillating signals. Application to image processing*, Appl. Math. Optim., 51 (2005), pp. 163–182, <https://doi.org/10.1007/s00245-004-0812-z>.
- [5] J.-F. AUJOL, G. AUBERT, L. BLANC-FÉRAUD, AND A. CHAMBOLLE, *Image decomposition into a bounded variation component and an oscillating component*, J. Math. Imaging Vis., 22 (2005), pp. 71–88, <https://doi.org/10.1007/s10851-005-4783-8>.
- [6] J.-F. AUJOL AND A. CHAMBOLLE, *Dual norms and image decomposition models*, Int. J. Comput. Vision, 63 (2005), pp. 85–104, <https://doi.org/10.1007/s11263-005-4948-3>.
- [7] J.-F. AUJOL, G. GILBOA, T. CHAN, AND S. OSHER, *Structure-texture image decomposition—modeling, algorithms, and parameter selection*, Int. J. Comput. Vision, 67 (2006), pp. 111–136, <https://doi.org/10.1007/s11263-006-4331-z>.
- [8] J.-F. AUJOL AND S. H. KANG, *Color image decomposition and restoration*, J. Vis. Commun. Image Rep., 17 (2006), pp. 916–928, <https://doi.org/10.1016/j.jvcir.2005.02.001>.
- [9] G. BELLETTINI, *Variational approximation of functionals with curvatures and related properties*, J. Convex Anal., 4 (1997), pp. 91–108, <https://eudml.org/doc/228786>.
- [10] P. BLOMGREN, T. F. CHAN, P. MULET, AND C.-K. WONG, *Total variation image restoration: Numerical methods and extensions*, in Proceedings of International Conference on Image Processing, Vol. 3, IEEE, 1997, pp. 384–387, <https://doi.org/10.1109/ICIP.1997.632128>.
- [11] A. BUADES, T. M. LE, J.-M. MOREL, AND L. A. VESE, *Fast cartoon + texture image filters*, IEEE Trans. Image Process., 19 (2010), pp. 1978–1986, <https://doi.org/10.1109/TIP.2010.2046605>.
- [12] A. CHAMBOLLE, *An algorithm for total variation minimization and applications*, J. Math. Imaging Vis., 20 (2004), pp. 89–97, <https://doi.org/10.1023/B:JMIV.0000011325.36760.1e>.
- [13] T. CHAN, S. ESEDOGLU, F. PARK, AND A. YIP, *Recent developments in total variation image restoration*, in Handbook of Mathematical Models in Computer Vision, N. Paragios, Y. Chen, and O. Faugeras, eds., Springer, Cham, 2005, pp. 17–31, https://doi.org/10.1007/0-387-28831-7_2.
- [14] T. F. CHAN, S. ESEDOGLU, AND F. E. PARK, *Image decomposition combining staircase reduction and texture extraction*, J. Vis. Commun. Image Rep., 18 (2007), pp. 464–486, <https://doi.org/10.1016/j.jvcir.2006.12.004>.

- [15] K. CHEN AND H. HAN, *Three-stage approach for 2D/3D diffeomorphic multi-modality image registration with textural control*, SIAM J. Imaging Sci., 17 (2024), pp. 1690–1728, <https://doi.org/10.1137/23M1583971>.
- [16] Q. CHEN AND V. KOLTUN, *A simple model for intrinsic image decomposition with depth cues*, in 2013 IEEE International Conference on Computer Vision, 2013, pp. 241–248, <https://doi.org/10.1109/ICCV.2013.37>.
- [17] A. J. CHORIN, T. J. HUGHES, M. F. McCACKEN, AND J. E. MARSDEN, *Product formulas and numerical algorithms*, Commun. Pure Appl. Math., 31 (1978), pp. 205–256, <https://doi.org/10.1002/cpa.3160310205>.
- [18] F. H. CLARKE, *Optimization and Nonsmooth Analysis*, SIAM, Philadelphia, 1990.
- [19] E. DE GIORGI AND L. AMBROSIO, *New functionals in calculus of variations*, in Nonsmooth Optimization and Related Topics, Springer, Cham, 1989, pp. 49–59.
- [20] L.-J. DENG, R. GLOWINSKI, AND X.-C. TAI, *A new operator splitting method for the Euler elastica model for image smoothing*, SIAM J. Imaging Sci., 12 (2019), pp. 1190–1230, <https://doi.org/10.1137/18M1226361>.
- [21] Q. DING, T. NIU, X. ZHANG, AND Y. LONG, *Image-domain multimaterial decomposition for dual-energy CT based on prior information of material images*, Med. Phys., 45 (2018), pp. 3614–3626, <https://doi.org/10.1002/mp.13001>.
- [22] D. L. DONOHO AND I. M. JOHNSTONE, *Adapting to unknown smoothness via wavelet shrinkage*, J. Amer. Statist. Assoc., 90 (1995), pp. 1200–1224, <https://doi.org/10.1080/01621459.1995.10476626>.
- [23] V. DUVAL, J.-F. AUJOL, AND L. VESE, *Projected gradient based color image decomposition*, in Scale Space and Variational Methods in Computer Vision: Second International Conference, SSVM 2009, Voss, Norway, Lecture Notes in Comput. Sci. 5567, Springer, Cham, 2009, pp. 295–306, https://doi.org/10.1007/978-3-642-02256-2_25.
- [24] E. ESSER, *Applications of Lagrangian-based alternating direction methods and connections to split Bregman*, CAM report, 9 (2009), 31, <https://ww3.math.ucla.edu/cam-reports-2001-2020/>.
- [25] L. C. EVANS, *Partial Differential Equations*, Grad. Stud. Math. 19, American Mathematical Society, Providence, RI, 2022.
- [26] J. B. GARNETT, P. W. JONES, T. M. LE, AND L. A. VESE, *Modeling oscillatory components with the homogeneous spaces $BMO^{-\alpha}$ and $\dot{W}^{-\alpha,p^*}$* , Pure Appl. Math. Q., 7 (2011), pp. 275–318, <https://dx.doi.org/10.4310/PAMQ.2011.v7.n2.a2>.
- [27] G. GILBOA AND S. OSHER, *Nonlocal operators with applications to image processing*, Multiscale Model. Simul., 7 (2009), pp. 1005–1028, <https://doi.org/10.1137/070698592>.
- [28] R. GLOWINSKI, *Finite element methods for incompressible viscous flow*, Handb. Numer. Anal., 9 (2003), pp. 3–1176, [https://doi.org/10.1016/S1570-8659\(03\)09003-3](https://doi.org/10.1016/S1570-8659(03)09003-3).
- [29] R. GLOWINSKI AND P. LE TALLEC, *Augmented Lagrangian and Operator-Splitting Methods in Nonlinear Mechanics*, SIAM, Philadelphia, 1989.
- [30] R. GLOWINSKI, S. J. OSHER, AND W. YIN, *Splitting Methods in Communication, Imaging, Science, and Engineering*, Springer, Cham, 2017.
- [31] R. GLOWINSKI, T.-W. PAN, AND X.-C. TAI, *Some facts about operator-splitting and alternating direction methods*, in Splitting Methods in Communication, Imaging, Science, and Engineering, R. Glowinski, S. J. Osher, and W. Yin, eds., Sci. Comput., Springer, Cham, 2016, pp. 19–94, https://doi.org/10.1007/978-3-319-41589-5_2.
- [32] Y. HE, S. H. KANG, AND H. LIU, *Curvature regularized surface reconstruction from point clouds*, SIAM J. Imaging Sci., 13 (2020), pp. 1834–1859, <https://doi.org/10.1137/20M1314525>.
- [33] Y. HU AND M. JACOB, *Higher degree total variation (HDTV) regularization for image recovery*, IEEE Trans. Image Process., 21 (2012), pp. 2559–2571, <https://doi.org/10.1109/TIP.2012.2183143>.
- [34] M. HUSKA, S. H. KANG, A. LANZA, AND S. MORIGI, *A variational approach to additive image decomposition into structure, harmonic, and oscillatory components*, SIAM J. Imaging Sci., 14 (2021), pp. 1749–1789, <https://doi.org/10.1137/20M1355987>.
- [35] Y. LAN, Z. LI, J. SUN, AND Y. XIANG, *DOSnet as a non-black-box PDE solver: When deep learning meets operator splitting*, J. Comput. Phys., 491 (2023), 112343, <https://doi.org/10.1016/j.jcp.2023.112343>.

- [36] T. M. LE AND L. A. VESE, *Image decomposition using total variation and $\text{div}(BMO)$* , Multiscale Model. Simul., 4 (2005), pp. 390–423, <https://doi.org/10.1137/040610052>.
- [37] N. LE BIHAN AND S. SANGWINE, *Color image decomposition using quaternion singular value decomposition*, in 2003 International Conference on Visual Information Engineering VIE 2003, IET, 2003, pp. 113–116, <https://doi.org/10.1049/cp:20030500>.
- [38] L. H. LIEU AND L. A. VESE, *Image restoration and decomposition via bounded total variation and negative Hilbert–Sobolev spaces*, Appl. Math. Optim., 58 (2008), pp. 167–193, <https://doi.org/10.1007/s00245-008-9047-8>.
- [39] H. LIU, J. LIU, R. H. CHAN, AND X.-C. TAI, *Double-well net for image segmentation*, Multiscale Model. Simul., 22 (2024), pp. 1449–1477, <https://doi.org/10.1137/24M1632103>.
- [40] H. LIU, X.-C. TAI, AND R. GLOWINSKI, *An operator-splitting method for the Gaussian curvature regularization model with applications to surface smoothing and imaging*, SIAM J. Sci. Comput., 44 (2022), pp. A935–A963, <https://doi.org/10.1137/21M143772X>.
- [41] H. LIU, X.-C. TAI, R. KIMMEL, AND R. GLOWINSKI, *A color elastica model for vector-valued image regularization*, SIAM J. Imaging Sci., 14 (2021), pp. 717–748, <https://doi.org/10.1137/20M1354532>.
- [42] H. LIU, X.-C. TAI, R. KIMMEL, AND R. GLOWINSKI, *Elastica models for color image regularization*, SIAM J. Imaging Sci., 16 (2023), pp. 461–500, <https://doi.org/10.1137/22M147935X>.
- [43] M. LYSAKER, A. LUNDERVOLD, AND X.-C. TAI, *Noise removal using fourth-order partial differential equation with applications to medical magnetic resonance images in space and time*, IEEE Trans. Image Process., 12 (2003), pp. 1579–1590, <https://doi.org/10.1109/TIP.2003.819229>.
- [44] S. MASNOU AND J.-M. MOREL, *Level lines based disocclusion*, in Proceedings 1998 International Conference on Image Processing. ICIP98 (Cat. No. 98CB36269), IEEE, 1998, pp. 259–263, <https://doi.org/10.1109/ICIP.1998.999016>.
- [45] S. MASNOU AND J.-M. MOREL, *On a variational theory of image amodal completion*, Rendiconti del Seminario Matematico della Universita di Padova, 116 (2006), pp. 211–252, http://www.numdam.org/item/RSMUP_2006__116__211_0.
- [46] Y. MEYER, *Oscillating patterns in image processing and nonlinear evolution equations: The fifteenth Dean Jacqueline B. Lewis Memorial Lectures*, Univ. Lecture Ser. 22, American Mathematical Society, Providence, RI, 2001.
- [47] D. MUMFORD, *Elastica and computer vision*, in Algebraic Geometry and its Applications: Collections of Papers from Shreeram S. Abhyankar’s 60th Birthday Conference, Springer, Cham, 1994, pp. 491–506.
- [48] R. M. NGUYEN AND M. S. BROWN, *Fast and effective L_0 gradient minimization by region fusion*, in Proceedings of the IEEE International Conference on Computer Vision, 2015, pp. 208–216.
- [49] S. ONO, *L_0 gradient projection*, IEEE Trans. Image Process., 26 (2017), pp. 1554–1564, <https://doi.org/10.1109/TIP.2017.2651392>.
- [50] S. OSHER, A. SOLÉ, AND L. VESE, *Image decomposition and restoration using total variation minimization and the H^{-1} norm*, Multiscale Model. Simul., 1 (2003), pp. 349–370, <https://doi.org/10.1137/S1540345902416247>.
- [51] M. T. PIMENTA AND M. MONTEMNEGRO, *Existence of a BV solution for a mean curvature equation*, J. Differential Equations, 299 (2021), pp. 51–64, <https://doi.org/10.1016/j.jde.2021.07.021>.
- [52] L. I. RUDIN, S. OSHER, AND E. FATEMI, *Nonlinear total variation based noise removal algorithms*, Phys. D, 60 (1992), pp. 259–268, [https://doi.org/10.1016/0167-2789\(92\)90242-F](https://doi.org/10.1016/0167-2789(92)90242-F).
- [53] J. SHEN, *Piecewise $H^{-1} + H^0 + H^1$ images and the Mumford–Shah–Sobolev model for segmented image decomposition*, Appl. Math. Res. Express, 2005 (2005), pp. 143–167, <https://doi.org/10.1155/AMRX.2005.143>.
- [54] J. SHEN, S. H. KANG, AND T. F. CHAN, *Euler’s elastica and curvature-based inpainting*, SIAM J. Appl. Math., 63 (2003), pp. 564–592, <https://doi.org/10.1137/S0036139901390088>.
- [55] X.-C. TAI, J. HAHN, AND G. J. CHUNG, *A fast algorithm for Euler’s elastica model using augmented Lagrangian method*, SIAM J. Imaging Sci., 4 (2011), pp. 313–344, <https://doi.org/10.1137/100803730>.
- [56] X.-C. TAI, H. LIU, AND R. CHAN, *PottsMGNet: A mathematical explanation of encoder-decoder based neural networks*, SIAM J. Imaging Sci., 17 (2024), pp. 540–594, <https://doi.org/10.1137/23M1586355>.

- [57] L. A. VESE AND S. J. OSHER, *Modeling textures with total variation minimization and oscillating patterns in image processing*, J. Sci. Comput., 19 (2003), pp. 553–572, <https://doi.org/10.1023/A:1025384832106>.
- [58] Y.-W. WEN, H.-W. SUN, AND M. K. NG, *A primal-dual method for the Meyer model of cartoon and texture decomposition*, Numer. Linear Algebra Appl., 26 (2019), e2224, <https://doi.org/10.1002/nla.2224>.
- [59] Y.-W. WEN, M. ZHAO, AND M. NG, *Cartoon and texture decomposition for color image in opponent color space*, Appl. Math. Comput., 414 (2022), 126654, <https://doi.org/10.1016/j.amc.2021.126654>.
- [60] X. WU, J. ZHENG, C. WU, AND Y. CAI, *Variational structure–texture image decomposition on manifolds*, Signal Process., 93 (2013), pp. 1773–1784, <https://doi.org/10.1016/j.sigpro.2013.01.019>.
- [61] J. XU, X. FENG, Y. HAO, AND Y. HAN, *Image decomposition and staircase effect reduction based on total generalized variation*, J. Syst. Eng. Electron., 25 (2014), pp. 168–174, <https://doi.org/10.1109/JSEE.2014.00020>.
- [62] L. XU, C. LU, Y. XU, AND J. JIA, *Image smoothing via L_0 gradient minimization*, ACM Trans. Graphics, 30 (2011), pp. 1–12, <https://doi.org/10.1145/2070781.2024208>.
- [63] M. YASHTINI AND S. H. KANG, *Alternating direction method of multiplier for Euler’s elastica-based denoising*, in Scale Space and Variational Methods in Computer Vision: 5th International Conference, SSVM 2015, Lège-Cap Ferret, France, Lecture Notes in Comput. Sci. 9087, Springer, Cham 2015, pp. 690–701, https://doi.org/10.1007/978-3-319-18461-6_55.
- [64] C.-H. ZHANG, *Nearly unbiased variable selection under minimax concave penalty*, Ann. Statist., 38 (2010), pp. 894–942, <https://doi.org/10.1214/09-AOS729>.
- [65] H. ZHANG, L. TANG, Z. FANG, C. XIANG, AND C. LI, *Nonconvex and nonsmooth total generalized variation model for image restoration*, Signal Process., 143 (2018), pp. 69–85, <https://doi.org/10.1016/j.sigpro.2017.08.021>.
- [66] W. ZHU, *A first-order image denoising model for staircase reduction*, Adv. Comput. Math., 45 (2019), pp. 3217–3239, <https://doi.org/10.1007/s10444-019-09734-5>.
- [67] W. ZHU AND T. CHAN, *Image denoising using mean curvature of image surface*, SIAM J. Imaging Sci., 5 (2012), pp. 1–32, <https://doi.org/10.1137/110822268>.